Delft University of Technology

Effect of epoxy resin addition on properties and corrosion behavior of sintered joints in power modules serviced offshore

Wang, Xinyue; Yang, Zhoudong; Wang, Boya; Chen, Wei; Zhang, Guoqi; Zhang, Jing; Fan, Jiajie; Liu, Pan

Important note
To cite this publication, please use the final published version (if applicable).
Please check the document version above.

Available online at www.sciencedirect.com

jmr&t
Journal of Materials Research and Technology

journal homepage: www.elsevier.com/locate/jmrt

Effect of epoxy resin addition on properties and corrosion behavior of sintered joints in power modules serviced offshore

Xinyue Wang [a], Zhoudong Yang [a,b], Boya Wang [c], Wei Chen [a],
Guoqi Zhang [d], Jing Zhang [e], Jiajie Fan [a], Pan Liu [a,f,g,*]

[a] Academy for Engineering & Technology, Fudan University, Shanghai 200433, China
[b] Laboratory of Advanced Materials, Fudan University, Shanghai 200433, China
[c] Laboratory of Advanced Materials, State Key Laboratory of Molecular Engineering of Polymers, School of Chemistry and Materials, Fudan University, Shanghai 200433, China
[d] Department of Microelectronics, Delft University of Technology, 2628 CD, Delft, the Netherlands
[e] Heraeus Materials Technology Shanghai Ltd., Shanghai 201108, China
[f] Yiwu Research Institute of Fudan University, Zhejiang Province 322000, China
[g] Research Institute of Fudan University in Ningbo, Zhejiang Province 315336, China

ARTICLE INFO

ABSTRACT

Power modules applied in offshore applications are facing risks of corrosion failures on die-attach materials due to high humidity and H_2S exposure. To investigate such corrosion behavior for sintered die-attach materials, we conducted a study with four groups of samples fabricated using copper and silver metal particles under different solvent systems. Such samples were firstly subjected to high-humidity-H_2S conditions for 168 h to simulate the harsh offshore environment. After undergoing corrosion, the primary compounds formed were CuO/Cu_2O and Ag_2S through SEM, XRD, and XPS analysis. Notably, the incorporation of epoxy resin into sintered copper joints resulted in a remarkable reduction in corrosion and a substantial improvement in electrical conductivity after the reaction. In contrast, while the addition of epoxy did not evidently reduce corrosion in silver joints, it did lead to a significant increase in shear strength. Furthermore, to gain further insights into the effect of epoxy resin on corrosion behavior, electrochemical analysis, and molecular dynamics simulations were conducted. Finally, the mechanical reliability of the corroded copper and silver joints was evaluated through thermal shock tests. In summary, sintered copper joints exhibited better anti-corrosion behaviors than sintered silver under high humidity and H_2S exposure, especially with the addition of epoxy resin. However, the corrosion products of sintered copper suffered from a sharp decrease in shear strength after thermal shock tests than sintered silver, which is probably due to the coefficient of thermal expansion mismatch.

* Corresponding author. Academy for Engineering & Technology, Fudan University, Shanghai 200433, China.
E-mail address: panliu@fudan.edu.cn (P. Liu).

1. Introduction

With the development of wide band-gap semiconductor materials, power modules fabricated with silicon carbide and gallium nitride are gradually being promoted into numerous applications [1—3], especially for applications under harsh working environments [4,5]. Consequently, these advancements present significant challenges to the surrounding electronic packaging materials [6]. Traditional lead-tin solders used to connect chips and substrates violate environmental regulations, while optimized lead-free solders suffer from low melting points, leading to creep failures during service [7,8]. Therefore, die-attach materials with improved reliability capable of withstanding high temperatures, currents, and high voltages are continuously being explored and developed [9].

Recent years, the Low-Temperature Joint Technology (LTJT) based on metal particle sintering has gained significant attention from both scholars [10,11] and industry. Silver is widely recognized for its excellent electrical and thermal conductivity [12], and sintered silver joints have exhibited superior reliability compared to common solder joints in various studies [13]. Additionally, copper exhibits similar properties to silver at a lower cost [14]. Consequently, sintered silver and sintered copper materials have been extensively investigated concerning sintering mechanism, process, and reliability [15,16]. However, studies on the corrosion behavior of these sintering materials, which aim to minimize high costs and maintenance difficulties in offshore applications, are still in their early stages.

With the continuous development of marine resources, power modules have broad application prospects in energy fields such as offshore wind power and photovoltaics [17,18]. This brings corrosion challenges caused by water, salt, and hydrogen sulfide (H_2S) to die-attach materials. While some research has focused on maritime environmental corrosion for sintered silver [19,20], limited work has been done to investigate the effect of H_2S. Hydrogen sulfide (H_2S) is a corrosive and harmful gas that exists in trace amounts in the air [21]. Due to human production activities, iron plants, and chemical fiber factories, a large amount of exhaust gas containing H_2S has been emitted in recent years, leading to a higher concentration of H_2S in the air [22,23]. It has been known that the aging of sintered metal joints accelerates with oxygen, water vapor, and H_2S [24], and corrosion failure plays an important role in reliability [25]. An example of the failure diagram of the power module in offshore wind power is shown in Fig. 1. Firstly, sintering materials vary in their corrosion mechanism due to their intrinsic properties. Silver is easily corroded by sulfides and is prone to electrochemical migration behavior with water vapor, while copper is highly susceptible to oxidation in the air [26,27]. Secondly, solvent systems of sintered materials have been found to be influential in reliability. Research has shown that the addition of epoxy resin to solder paste is effective for water vapor insulation, thereby alleviating the short circuit problem caused by metal whisker formation [28]. Jung et al. applied epoxy resin to the sintered silver paste and copper paste for high shear strength and oxidation resistivity, particularly for sintered copper under a high-temperature storage test [29,30]. They also pointed out that a limited amount of epoxy (e.g. 10 wt %) shared a limited effect on the reduction of electrical conductivity [30]. However, the anti-corrosion effect of solvent systems on sintered copper or sintered silver joints aged in high-humidity-H_2S environments has been barely reported.

In this study, four groups of pressure-assisted sintered samples were firstly fabricated, namely copper paste, epoxy-added copper paste, silver paste, and epoxy-added silver paste. The samples, after aging in high-humidity-H_2S
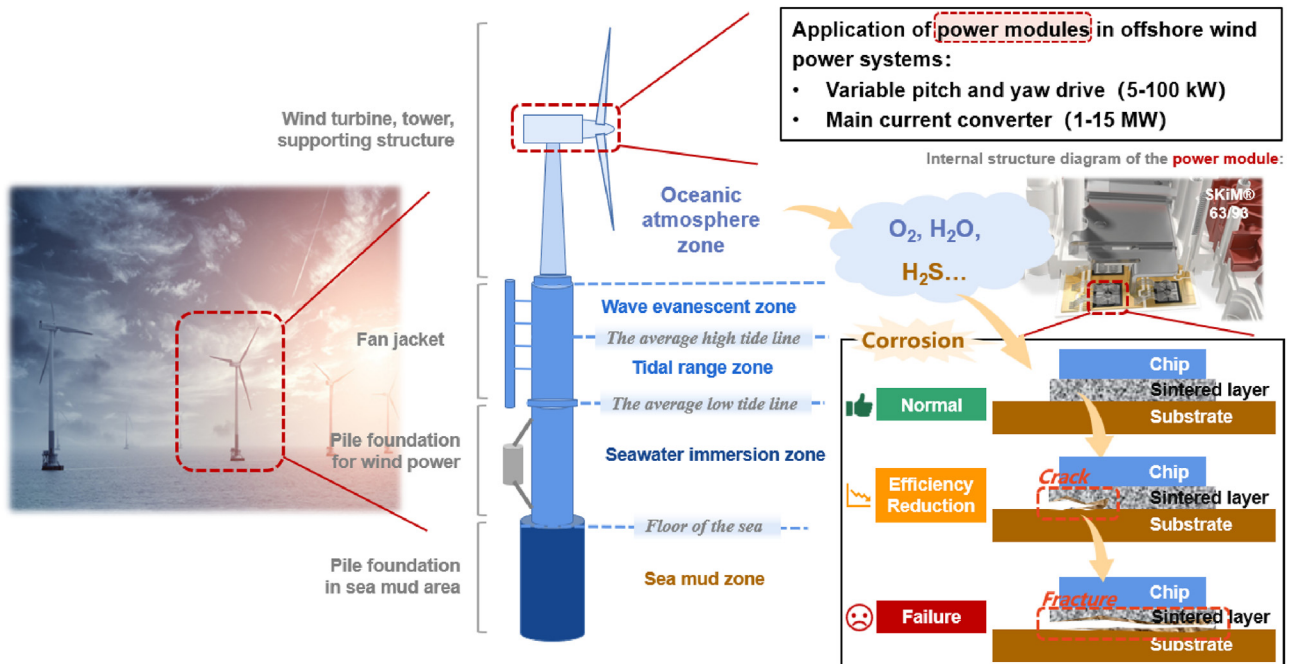

Fig. 1 — The failure diagram of the power module in offshore wind power application.
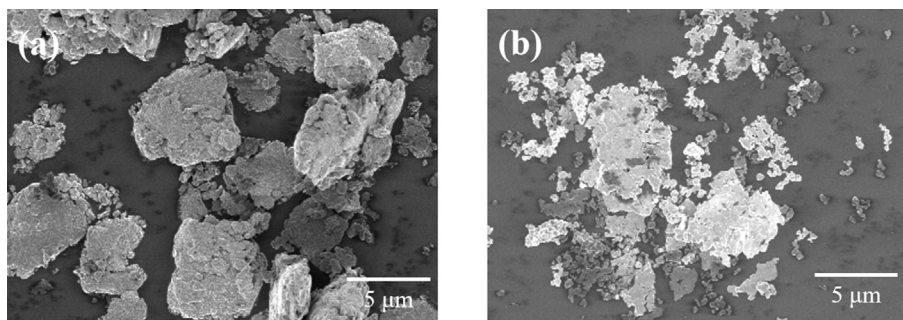
Fig. 2 — SEM photos of (a) Cu particles and (b) Ag particles.

conditions, were compared and analyzed through their appearance, weight, shear strength, cross-section, and resistance before and after the corrosion. After that, the corrosion mechanism of each group of joints was further analyzed through various techniques, including Scanning Electron Microscopy with Energy Dispersive X-ray Spectroscopy (SEM/EDS), X-Ray Diffraction (XRD), X-ray Photoelectron Spectroscopy (XPS), and electrochemistry technique. Additionally, molecular dynamics (MD) simulation combined with a force field (ReaxFF) was used to investigate the atomistic details during corrosion. Finally, for a deep understanding of the reliability of corroded sintered joints during operation, the sintered copper and silver joints were evaluated for thermal shock tests. The results of this work provide insights into the research and development of anti-corrosion sintered joints for power modules of offshore applications.

2. Experiments and methodology

2.1. Materials and corrosion test

2.1.1. Preparation of sintering pastes

Flake copper powder and silver powder, with diameters ranging from 1 to 3 μm, were selected for this study from Guangzhou Hongwu Material Technology, as shown in Fig. 2. Two solvents were prepared to investigate the anti-corrosion effect of epoxy-added sintering paste. One solvent was epoxy-free, primarily consisting of a mixture of terpineol and polyethylene glycol (Shanghai Aladdin Biochemical Technology). The other solvent was doped with an epoxy system and compound thinner from Heraeus GmbH. The epoxy system constituted one-third of the solvent mass and included epoxy resin sourced from KUKDO Chemical (Kunshan), a curing agent (methyl-tetrahydro phthalic anhydride), and an accelerator (2-Ethyl-4-methylimidazole) for epoxy obtained from Jiaxing Nanyang Wanshixing Chemical. The mass ratio of resin, curing agent, and accelerator was 10:9:0.9. The thermal performance of these solvents was shown in Fig. 3. Thermogravimetric Analysis-Differential Scanning Calorimetry (TG-DSC) testing was carried out using an SDT-Q600 Synchronous Thermal Analyzer (TA Instrument Company, New Castle, DE) under a nitrogen atmosphere, and heated to 400 °C at a ramp rate of 10 °C/min. The results showed that the epoxy-free solvent did not exhibit any obvious endothermic or exothermic phenomenon before 250 °C, which was the sintering temperature set in this study. Additionally, its weight decreased around 140 °C, with the mass loss reaching 42.1% at 250 °C, as shown in Fig. 3(a). Conversely, the mass loss of the epoxy-added solvent was 52.8% at 250 °C, indicating that organic residues were present in both joints after sintering. Simultaneously, the heat flow curve of the epoxy-added solvent in Fig. 3(b) showed an endothermic peak after the beginning of the heating process, which was caused by the curing of the resin. The analysis of solvents not only
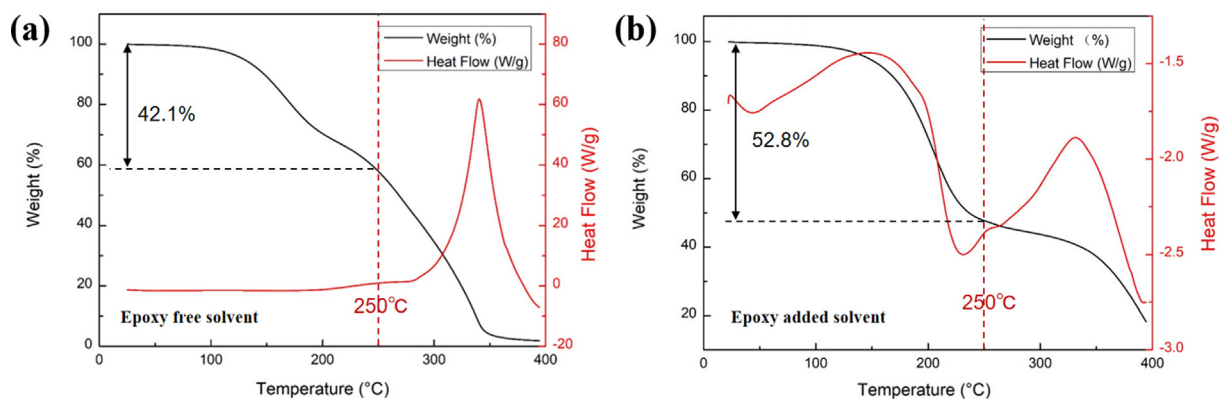

Fig. 3 — Thermal performance analysis of (a) epoxy-free solvent and (b) epoxy-added solvent.

Table 1 − Overview of the pastes prepared in this work.

Paste	Particles	Solvent
Cu-1	Copper	Epoxy free (5 wt% terpineol+10 wt% polyethylene glycol)
Ag-1	Silver	Epoxy free (5 wt% terpineol+10 wt% polyethylene glycol)
Cu-2	Copper	Epoxy added (5 wt% epoxy+10 wt% thinner)
Ag-2	Silver	Epoxy added (5 wt% epoxy+10 wt% thinner)

illustrated the degree of organic residues but also provided the basis for setting parameters in the subsequent pre-drying process.

After that, four types of paste were prepared, and the solvent accounted for 15% of the total weight of the paste. The composition information of the pastes is shown in Table 1. Agate mortar combined with a centrifuge was applied to mix particles and the solvent. The dispersion time of each paste was more than 40 min.

2.1.2. Preparation of sintered samples

In this work, pressure-assisted sintered samples of each paste were prepared for shear strength analysis and discrete sintered samples with cylinder shapes were prepared for electrical conductivity analysis. As shown in Fig. 4(a), the preparation process involved stencil printing on Direct Bonding Copper (DBC) substrates, pre-drying in a nitrogen atmosphere, and the application of dummy chips with sizes of 2 mm × 2 mm × 0.25 mm to replace the actual power chips, which were then placed over the sintering paste. The back of the dummy chips has a silver coating with a thickness greater than 0.1 μm. The sandwich structure was sintered under the pressure of 20 MPa at 250 °C for 900 s, using Boschman Sinterstar Innovate-F-XL. Finally, sintered joints were successfully fabricated. To test the conductivity of the sintered layer and obtain the corrosion products of the sintered material, discrete sintered samples with cylinder shapes were produced at the same time. Similar to the process for preparing sintered joints, cylindrical sintered samples were fabricated with approximately 12.7 mm in diameter and 0.5−1.5 mm in thickness on ceramic substrates, as shown in Fig. 4(b). It is worth mentioning that the solvent without epoxy was dried at 140 °C for 20 min, and the solvent containing epoxy was dried at 90 °C for 15 min, according to the thermal analysis of the

two solvents in Section 2.1. The specific sintering process of each paste is shown in Table 2. The purpose of setting the pre-drying step is to evaporate part of the low-boiling organic matter as much as possible, which reduces the organic residuary in the joint after the final sintering is completed.

2.1.3. Hydrogen sulfide gas corrosion experiments

To investigate the anti-corrosion effect of sintered copper or sintered silver joints with the addition of epoxy, four groups of samples were aged in high-humidity-H_2S conditions using Gas Corrosion Test Equipment (YAMASAKI, GH-180). The temperature was maintained at 45 °C during the 168-h corrosion period. The aging process was accelerated by maintaining high humidity at 85% RH and introducing 100 parts-per-billion (ppb) of H_2S into the environment. All four groups of samples were aged simultaneously under these conditions.

2.2. Characterization methodology

2.2.1. Characterization of the properties of the joints

To compare the macro changes of various samples before and after corrosion, an Optical Microscope (OM, KEYENCE) was applied to record the appearance of the samples. In terms of shear strength measurement, Push-pull Testing Machine (DAGE) was employed. A four-probe tester (RTS-8) was utilized to analyze electrical conductivity change at a temperature of (25 ± 5)°C and 65%RH.

2.2.2. Characterization of the corrosion products

To investigate the difference in corrosion mechanism among joints, Scanning Electron Microscopy with Energy Dispersive X-ray Spectroscopy (SEM/EDS, Zeiss) was introduced to observe and analyze the element distribution of the surface
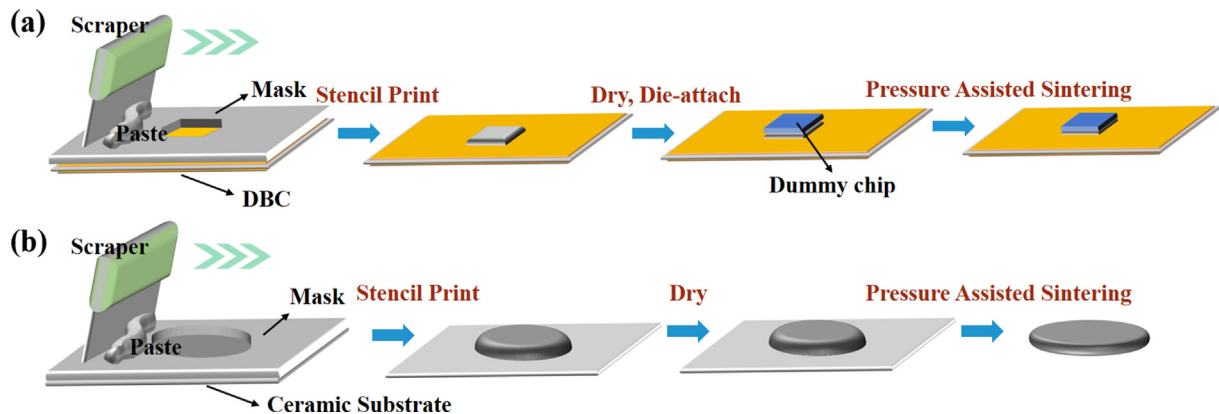
Fig. 4 − Schematic diagram of (a) sintered joint sample preparation and (b) cylindrical sintered sample preparation.

Table 2 – Overview of the sintering processes in this work.		
Paste	Pre-drying	Pressure assisted sintering
Cu-1 (epoxy free)	140 °C, 20 min, Nitrogen atmosphere	20 MPa, 15 min, 250 °C, Nitrogen atmosphere
Ag-1 (epoxy free)	140 °C, 20 min, Nitrogen atmosphere	20 MPa, 15 min, 250 °C, Nitrogen atmosphere
Cu-2 (epoxy added)	90 °C, 15 min, Nitrogen atmosphere	20 MPa, 15 min, 250 °C, Nitrogen atmosphere
Ag-2 (epoxy added)	90 °C, 15 min, Nitrogen atmosphere	20 MPa, 15 min, 250 °C, Nitrogen atmosphere

and cross-sections. Subsequently, the crystal structure change of the sintered samples was characterized by an X-ray Diffractometer (XRD, BRUKER) using Cu Kα radiation ($\lambda = 0.15418$ nm). An X-ray Photoelectron Spectroscopy (XPS, Thermo Fischer, ESCALAB Xi+) equipped with an Al Kα excitation source ($h\nu = 1486.6$ eV) was employed to study the chemical structure of elements Cu, Ag, C, O, and S in sintered samples after corrosion.

2.2.3. Electrochemical measurement

The corrosion behavior of the samples was characterized by potentiodynamic polarization curves and electrochemical impedance spectroscopy (EIS), operated on the EC-Lab electrochemical workstation (Biologic VSP-3e) in the corrosive solution at 45 ± 1 °C with a conventional three-electrode cell. Prior to the electrochemical measurements, the solutions were saturated with corrosion gas by being in contact with air and H_2S gas. However, after the measurements, the electrolyte was no longer aerated. The potentiodynamic polarization curves were measured within the range of -0.4 V to 0.3 V (vs. SSCE) at a scan rate of 120 mV/min. For the EIS test, we applied the frequency range from 100 kHz to 100 MHz with a disturbance amplitude of 5 mV.

2.2.4. Thermal shock tests

Thermal shock behavior is very important when evaluating die-attach for high-power applications. In this work, the JESD22-A104 standard was selected, which lasted 500 temperature cycles within a range of -50 to 150 °C, with a cycling rate of 2 cycles per hour.

2.3. MD simulation methods and details

2.3.1. ReaxFF-MD simulation

It is challenging to track the atomic-level changes during the corrosion process in experiments. Hence, MD simulations based on the Large-scale Atomic/Molecular Massively Parallel Simulator (LAMMPs) was considered as an ideal tool to shed light on the corrosion mechanism. The Open Visualization Tool (OVITO) software was utilized to realize three-dimensional visualization of the calculation results.

Since the corrosion process involves chemical reactions, the ReaxFF was developed by Van Duin et al. [31] including bonding and breaking chemical bonds was utilized in this work. Similar to the nonreactive force field, the total energy of the ReaxFF force field is divided as follows:

$$E_{system} = E_{bond} + E_{over} + E_{under} + E_{val} + E_{pen} + E_{tors} + E_{conj} + E_{vdWaals} + E_{Coulomb}$$

(1)

where E_{bond} is the bond energy; E_{over} is the correction term of over coordination; E_{under} is the correction term of under-coordination; E_{val} is the bond angle term; E_{pen} is the extra energy loss of the two double bond systems; E_{tors} is the torsion angle term, E_{conj} is the conjugate energy. The above energy terms are related to the order of the bond and the environment. And the last two non-bonded terms are the van der Waals force term ($E_{vdWaals}$) and the Coulomb force term ($E_{Coumolb}$).

2.3.2. Simulation details

To simulate the effect of adding epoxy resin on the corrosion behavior, a three-layer composite system was established. The first layer consisted of a corrosive gas mixture containing oxygen, water, and hydrogen sulfide. The second layer was an organic layer, which was simplified based on the thermogravimetric analysis conducted in Section 2.1.1. The remaining organic matter was approximated to polyethylene glycol (Cu-1, Ag-1) and epoxy resin (Cu-2, Ag-2), respectively. The third layer was a metal layer, comprising silver (Ag-1, Ag-2) and copper (Cu-1, Cu-2), respectively. The simulation cell dimensions were approximately 52 Å × 52 Å × 65 Å and contained 9728 atoms (Ag-1), 10,656 atoms (Ag-2), 11,440 atoms (Cu-1), and 12,368 atoms (Cu-2), respectively.

To mimic the conditions of H_2S gas corrosion, the system temperature was maintained at 318 K to investigate the reaction-diffusion of the corrosive gas. The NVT ensemble was employed to simulate the corrosion process. The simulation time step was set as 1 fs, the number of steps was 5×10^6, and the total duration was 500 ps. In the simulation process, periodic boundary conditions were applied in the x, y, and z directions. The temperature was controlled with the nose-Hoover thermostat.

3. Results and discussion

3.1. Analysis of properties changes after corrosion

3.1.1. Appearance and weight analysis

During the corrosion process, significant changes were observed in both the surface and weight of the specimens. To accurately record these changes, four groups of sintered joints were fabricated on DBC substrates using four different types of sintering paste. Each group consisted of 2 DBC substrates and 6 sintered joints with dummy chips on each sample. To document the condition of the samples before and after corrosion, optical micrograph photos were taken and presented in Fig. 5. As illustrated in Fig. 5(a) and (b), the joints sintered with paste Cu-1 and paste Ag-1 were surrounded by
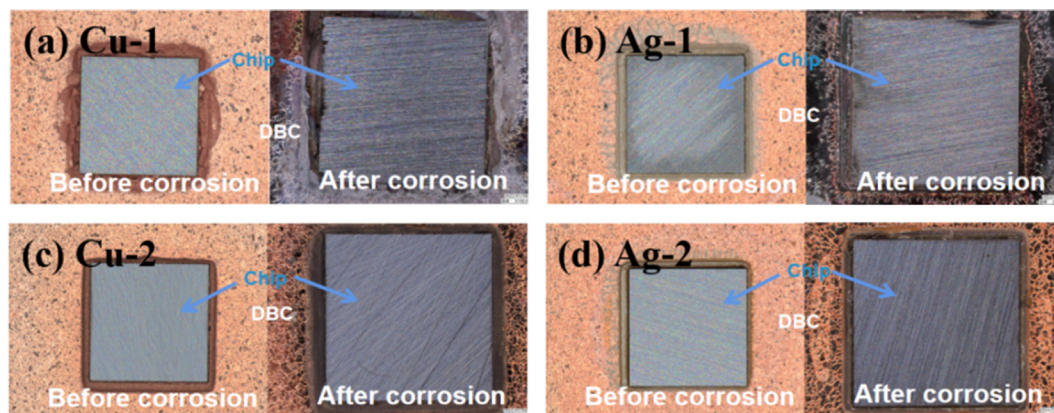
Fig. 5 − OM photos of the surface before and after corrosion (a) Cu-1; (b) Ag-1; (c) Cu-2; (d) Ag-2.

dark corrosion residues. Notably, the epoxy-added solvent system provided significant protection to the substrate surface around the chip compared to the epoxy-free solvent system. This protective effect was clearly observed in Fig. 5(c) and (d), where the copper substrate around the chips was protected while the other substrate areas were corroded. The results of this study demonstrated that the epoxy resin exhibited an excellent protective effect on the edge of the sintered layer and the surrounding substrate.

In addition, weight change was selected as another indicator of the occurrence of corrosion due to the formation of oxides and sulfides. Table 3 recorded the weight change of samples before and after corrosion. Moreover, the average weight change of the four groups of samples was compared in Fig. 6. The data showed that the weight of the samples increased after aging. Specifically, the average weight of Cu-1, Ag-1, Cu-2, and Ag-2 increased by 0.0217%, 0.0322%, 0.0200,% and 0.0175%, respectivel. In combination with the inspected surface changes, it can be concluded that epoxy provided effective corrosion protection for the sintered joints. However, when considering DBC boards with joints, the macroscopic mass increment can be influenced by various factors. Firstly, based on the OM photos, it is observed that a significant area of exposed copper on the DBC board's surface undergoes corrosion and appears blackened. This factor also contributes to the increase in mass. Secondly, the presence of water-stained patterns of varying degrees on the substrate surface, resulting from corrosion in a high-humidity environment, also cause variations in mass. Furthermore, the quantity of sintered material utilized in the joint is relatively small, and any excess slurry could act as a protective barrier, slowing
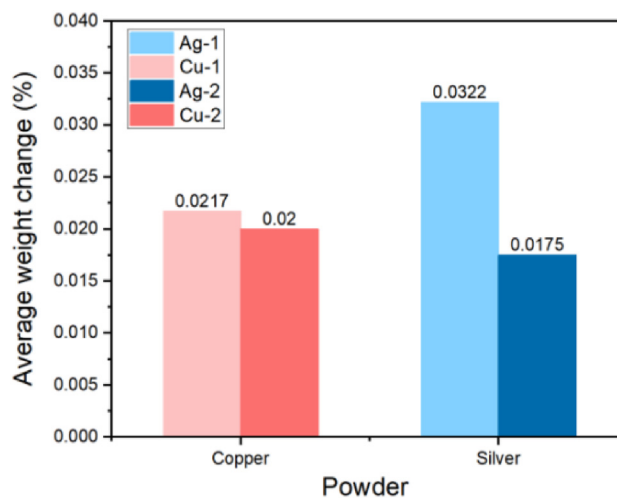

Fig. 6 − Comparison of the average weight change of the samples.

down the corrosion process of the copper substrate surrounding the epoxy joint. As a result, it leads to a reduction in mass gain after corrosion. Therefore, we consider that the mass increment observed in DBC with joints serves as a direct indicator of corrosion. However, it certainly could not be solely relied on to determine the degree of corrosion when studying sintered materials. It is crucial to consider additional factors that may influence the macroscopic mass changes in such systems, such as corrosion of the substrate and water stain residue.

Table 3 − Record of the weight change of samples before and after corrosion.

| Sintered joints (with DBC)	Sample 1 Before Corrosion (g)	Sample 1 After Corrosion (g)	Sample 2 Before Corrosion (g)	Sample 2 After Corrosion (g)	Average Weight Change (%)
Cu-1	5.7543	5.7553	5.7461	5.7476	0.0217
Ag-1	5.7559	5.7579	5.7229	5.7246	0.0322
Cu-2	5.7597	5.7608	5.7399	5.7411	0.0200
Ag-2	5.7257	5.7268	5.7242	5.7251	0.0175
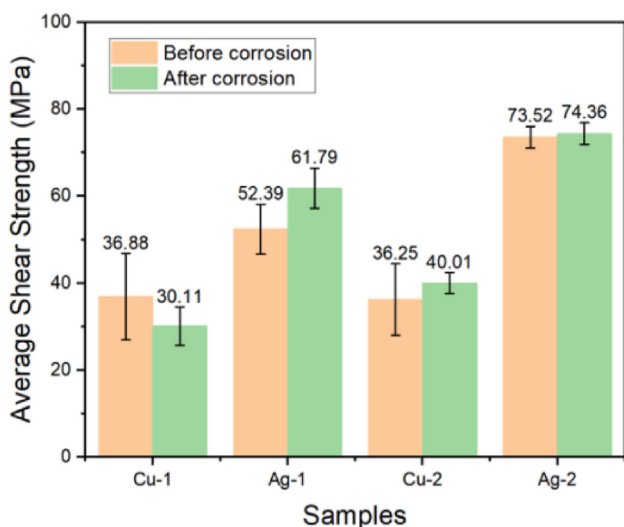
Fig. 7 – Average shear strength of the sintered joints before and after corrosion.

3.1.2. Shear strength analysis

Shear strength is the most commonly applied metric for evaluating the mechanical properties of joints. The average shear strength of the sintered joints before and after corrosion was compared in Fig. 7. The Cu-1 samples showed a clear decrease in shear strength, from 36.88 MPa to 30.11 MPa, while the Cu-2 samples exhibited an increase of 10.4%, which is probably related to the addition of epoxy resin. For the Ag-1 samples, the shear strength increased by 17.95%, which was more significant compared to the Ag-2 samples which only increased by 1.1%. In general, silver sintered joints studied in

this work exhibited a higher shear strength before and after the corrosion. Though the shear strength of copper joints in this work could not reach the same level, they remained over 30 MPa both before and after the corrosion, which are usually considered fair enough for die attach investigations.

At the same time, OM images of the shear fractured surface before and after corrosion were presented in Fig. 8. The fracture modes (Fig. 8(e)) of the sintered joints in the Ag-1 and Ag-2 samples were consistent before corrosion, exhibiting adhesive fractures at the substrate. This indicated that the internal sintering connection strength of silver was greater than the connection strength between the sintered body and the substrate, thereby not affecting the fracture mode. However, upon the addition of epoxy, the bonding effect between the sintered substrates was significantly enhanced, resulting in a fracture still occurring at the substrate, but with improved shear strength. Conversely, in the case of the copper joints, the fracture mode changed from cohesive fracture to adhesive fracture at the substrate after the addition of epoxy. This change indicated that the matrix connection was insufficient, while the connection at the substrate was stronger, leading to internal failure in Cu-1. With the addition of epoxy, the internal connection was strengthened, enabling it to withstand shear forces exceeding those of the substrate, resulting in fractures occurring at the substrate. However, the addition of epoxy did not improve the connection between the sintered copper and the substrate, resulting in no significant improvement in the shear performance of Cu-2. After corrosion, the fracture patterns of Cu-1, Ag-1, and Ag-2 sintered joints remained unchanged. However, the fracture failure mode of the Cu-2 sintered joint after corrosion was altered, with a combination of substrate adhesive fracture and internal fracture. This phenomenon is presumed to be caused by a
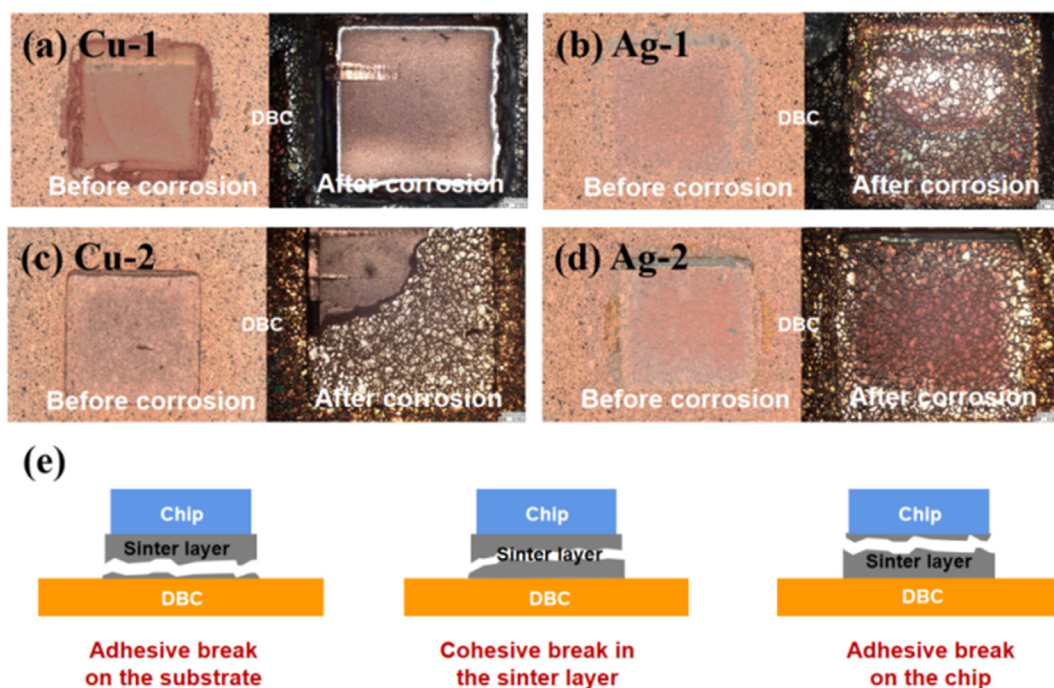
Fig. 8 – OM photos of the shear fractured surface before and after corrosion (a) Cu-1; (b) Ag-1; (c) Cu-2; (d) Ag-2. (e) Schematic diagram of the fracture modes.

Table 4 — Electrical conductivity after corrosion.	
Cylindrical sintered sample	Electrical Conductivity After Corrosion (s/cm)
Cu-1	$7.16*10^4$
Ag-1	$2.36*10^5$
Cu-2	$7.99*10^4$
Ag-2	$2.13*10^5$

decrease in the internal strength of the sintered body due to the presence of corrosion products.

By integrating the analysis of surface changes, weight changes, and fracture modes, we speculated that the characteristics and formation of corrosion products were the primary factors contributing to the variation in shear strength. The decline in the shear strength of the Cu-1 joint could be attributed to the presence of a significant quantity of copper corrosion products in the absence of epoxy protection. Conversely, in the case of the epoxy-protected Cu-2 joints, a minimal amount of copper corrosion products that fill the pores was likely responsible for the slight increase in strength. However, for the silver joints, it was plausible that the greater quantity of corrosion products generated under the prevailing corrosion conditions was the reason behind the observed increase in joint strength.

3.1.3. Electrical conductivity analysis

As a type of electronic packaging material that connects chips and substrates, the sintered layer is required to carry high currents. Therefore, it is crucial to evaluate the changes in the electrical conductivity of the connection material after undergoing corrosion. As detailed in Section 2.2, standard discrete sintered samples with cylinder shapes were prepared under the same process conditions and subjected to the same corrosion conditions mentioned above for the purpose of conducting electrical conductivity tests. The electrical conductivity of the samples after corrosion was presented in Table 4. The conductivity of sintered silver was higher than that of sintered copper. This observation is consistent with the electrical conductivity of bulk silver (6.3×10^5 S/cm) being superior to that of bulk copper (5.9×10^5 S/cm) [12,14]. The existence of pores in the sintered samples caused a reduction in their electrical conductivity. Prior research indicates that epoxy resin typically reduces conductivity, which is why the conductivity of Ag-1 (2.36×10^5 S/cm) was higher than that of Ag-2 (2.13×10^5 S/cm). However, the electrical conductivity of Cu-1 (7.16×10^4 S/cm) was lower than that of Cu-2 (7.99×10^4 S/cm), most likely due to the product having low electrical conductivity after corrosion. Further analysis was conducted in Section 3.3.

3.2. Cross-section analysis

To investigate the corrosion conditions in chip connection structures, cross-sectional samples were prepared and observed using Scanning Electron Microscopy (SEM). Cross-section SEM photos were presented in Fig. 9. Fig. 9(a) revealed severe corrosion along the edge of Cu-1, as well as collapse at the corner of the cross-section sample, ultimately leading to decreased shear strength. Additionally, black corrosion products were observed on the edge of Ag-1. The presence of cracks on the fracture surface is shown in Fig. 9(b). However, adding epoxy resin to the paste resulted in intact joint edges in Cu-2 and relatively complete cross-section edges in Ag-2 with only a slight burst (Fig. 9(c) and (d)).

3.3. Analysis of the corrosion products

The effects of high-humidity (85% RH)-H_2S (100 ppb) conditions on the appearance, weight, shear strength, electrical conductivity, and cross-section of sintered samples were
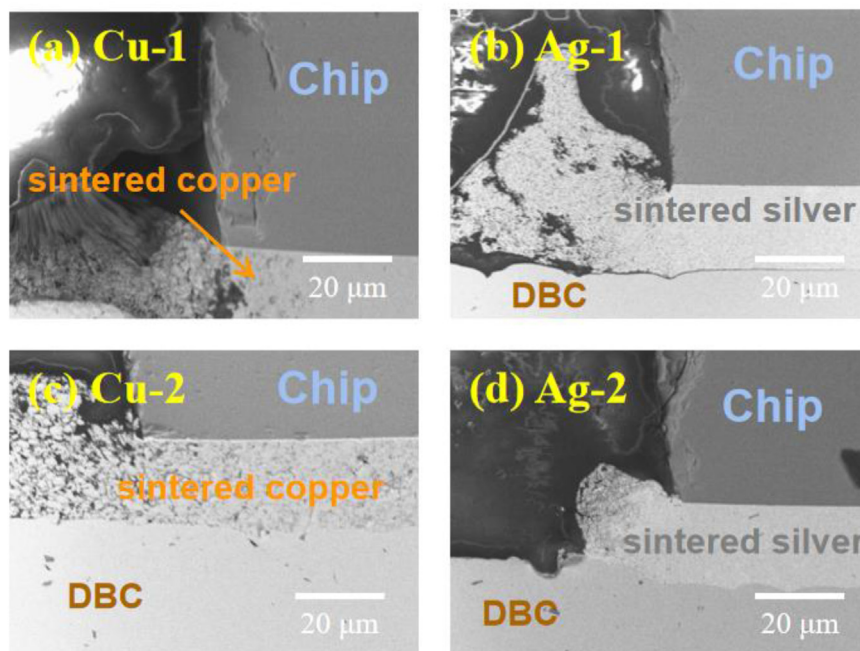
Fig. 9 — Cross section SEM photos of the joints after corrosion (a) Cu-1; (b) Ag-1; (c) Cu-2; (d) Ag-2.
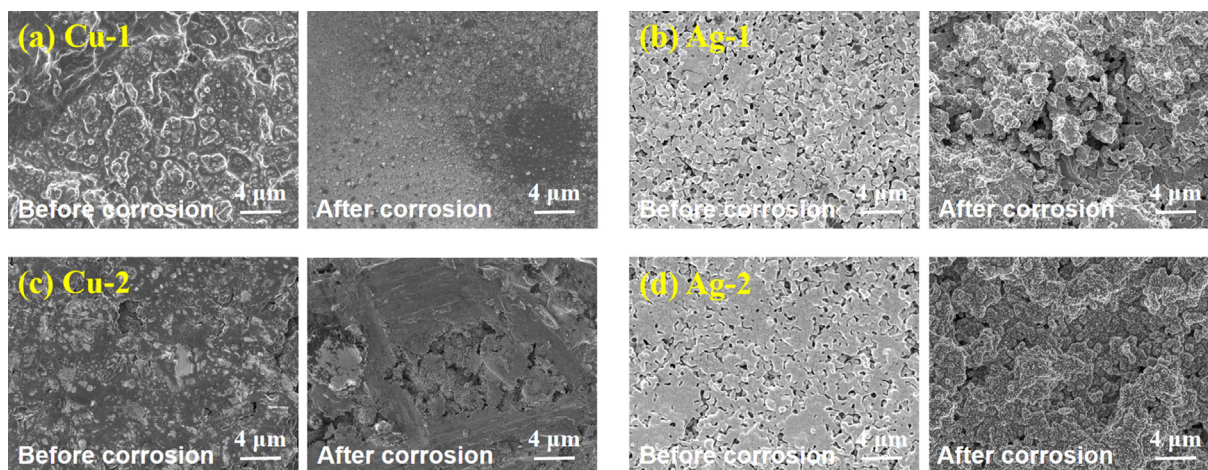
Fig. 10 — Surface SEM photos of the cylindrical sintered samples fabricated by (a)Cu-1; (b)Ag-1; (c)Cu-2 and (d)Ag-2 pastes.

previously reported and analyzed. Further investigations were conducted to shed light on the underlying mechanisms.
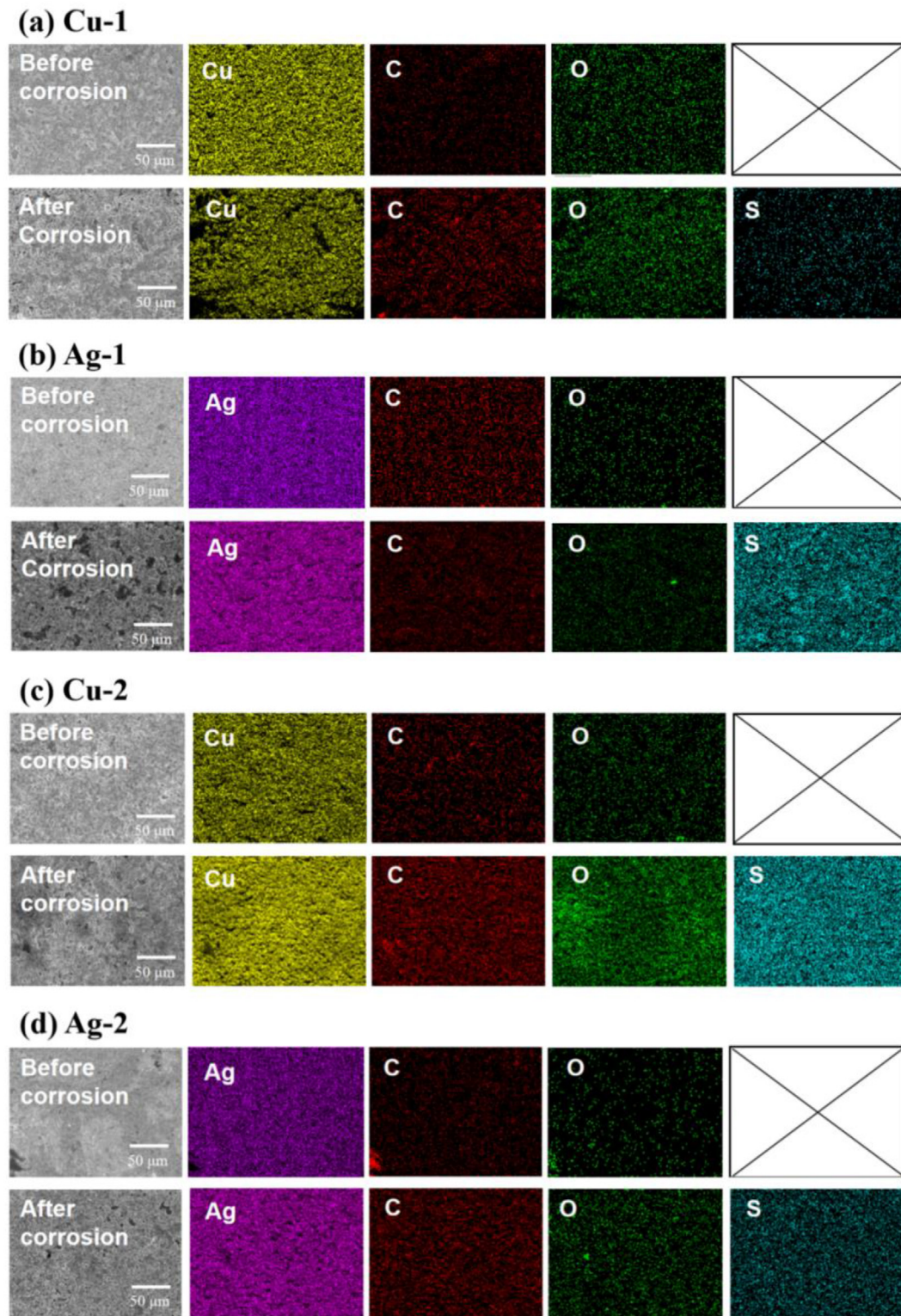
Firstly, the surface of the cylindrical sintered samples was examined through SEM, and the surface morphology characterization was presented in Fig. 10. Comparing the images, it was observed that a considerable amount of loose corrosion products appeared on the surface of the Cu-1 sample after the reaction, as shown in Fig. 10(a). In contrast, the surface of the Cu-2 sample was well coated with epoxy resin, as illustrated in Fig. 10(c). Moreover, as depicted in Fig. 10(b) and (d), there was no significant difference in the surface morphology of the Ag-1 and Ag-2 samples after the reaction, although traces of resin coating were evident on the surface of the Ag-2 sample. These morphological differences indicated that epoxy resin had the potential to effectively protect sintered copper from corrosion. However, the addition of an epoxy-based solvent had a minimal anti-corrosion effect on sintered silver.

Secondly, Energy Dispersive X-ray Spectroscopy (EDS) was employed to investigate the elemental composition of the surface. Table 5 listed the surface element distribution, while Fig. 11 displayed the elemental mapping images of the surface of cylindrical sintered samples before and after corrosion. The elemental analysis revealed that the element that increased significantly after corrosion on the surface of sintered copper samples was oxygen. Furthermore, the proportion of oxygen distribution on the surface of the sintered sheet without the addition of epoxy resin increased from 5.6 wt% to 17.6 wt%, which was over three times that of the epoxy-added sample, which only showed a 3.6 wt% increase. Thus, we inferred that the corrosion products of copper joints were mainly copper oxides, and the addition of epoxy resin effectively prevented the formation of oxides during the corrosion process. Concerning the sintered silver samples, the mass-specific gravity of the sulfur element showed a more apparent change. The sulfur element on the surface of Ag-1 and Ag-2 etched samples increased by 5.2 wt% and 5.7 wt%, respectively. These results demonstrated that the corrosion product on the silver surface was sulfide, and the effect of epoxy resin on the surface corrosion resistance was insignificant.

Next, X-ray diffraction (XRD) was performed to identify the corrosion products of each cylindrical sintered sample. The product resulting from sintering copper in an atmosphere of hydrogen sulfide and water vapor was indexed to a mixture of CuO and Cu_2O (JCPDS: 02-1076), as illustrated in Fig. 12(a). Small peaks of the mixture phase of CuO and Cu_2O were observed in the reaction product of the Cu-1 sample based on the sintered copper (JCPDS: 04-0836). Notably, the peaks of the Cu-2 sample after corrosion were nearly identical to the initial surface. The results confirmed the protective effect of epoxy resin on sintered copper. Furthermore, as presented in Fig. 12(c), possible reactions of the sintered copper under high-humidity (85% RH)-H_2S (100 ppb) corrosion conditions were listed, and the corresponding reaction energy changes were calculated. The data of ΔG utilized in the calculation were obtained from Lange's Handbook of Chemistry [32]. Based on the change of Gibbs free energy, the oxide energy of copper was lower than that of sulfide. Thus, the main product was oxide, which was in agreement with the results of XRD and EDS. In contrast, both samples of sintered silver after corrosion exhibited distinct phase peaks of Ag_2S (JCPDS: 14-0072), as shown in Fig. 12(b), and the Ag_2S peaks of the Ag-2 sample were slightly lower. The test results of XRD were consistent with the EDS analysis, indicating that Ag_2S was highly active, and the protective effect of epoxy on sintered silver was not apparent. When combined

Table 5 — EDS results of material compositions for the surface of cylindrical sintered samples before and after corrosion.

Sintered samples	Cu (%wt)	Ag (%wt)	C (%wt)	O (%wt)	S (%wt)
Cu-1-Before corrosion	79.2	—	21.5	5.6	—
Cu-1-After corrosion	46.1	—	35.0	17.6	1.3
Ag-1-Before corrosion	—	94.8	3.0	2.3	—
Ag-1-After corrosion	—	82.5	7.4	5.0	5.2
Cu-2-Before corrosion	77.9	—	18.7	3.3	—
Cu-2-After corrosion	64.4	—	24.8	7.0	3.8
Ag-2-Before corrosion	—	93.0	4.4	2.6	—
Ag-2-After corrosion	—	82.6	9.7	2.0	5.7

Fig. 11 − EDS elemental mapping images of the surface of cylindrical sintered samples before and after corrosion (a) Cu-1; (b) Ag-1; (c) Cu-2 and (d) Ag-2.

with the calculation results of the Gibbs free energy of possible products in Fig. 12(d), the free energy of the process from silver to silver sulfide was significantly reduced, implying that silver sulfide was the main product under corrosion conditions. The

calculated results were in accordance with the XRD and EDS characterization outcomes.

Subsequently, the corroded surface of the samples was further analyzed using X-ray photoelectron spectroscopy

(XPS). Fig. 13(a)–(d) showed the Cu 2p, C 1s, O 1s, and S 2p XPS spectra of sintered copper after being exposed to 85%RH humidity and 100 ppb H_2S at 45 °C for 168 h. From the Cu 2p XPS spectrum in Fig. 13(a), the Cu 2p peak shape on the surface of the Cu-1 sample had a strong satellite peak, indicating the presence of divalent copper compounds on the surface [33]. Conversely, in the results of the Cu-2 sample, the satellite

peak disappeared, indicating that the surface was almost unreacted. Further information about the products of Cu-1 after the reaction was determined by analyzing the XPS spectra of O 1s (Fig. 13(c)) and S 2p (Fig. 13(d)). The peak at 530.9 eV in the O 1s XPS spectrum belonged to the Cu–O bond of oxides mixture of copper, which corresponds to the results of XRD [34]. However, peaks at 161.1 eV (S $2p_{3/2}$) and 162.5 eV (S
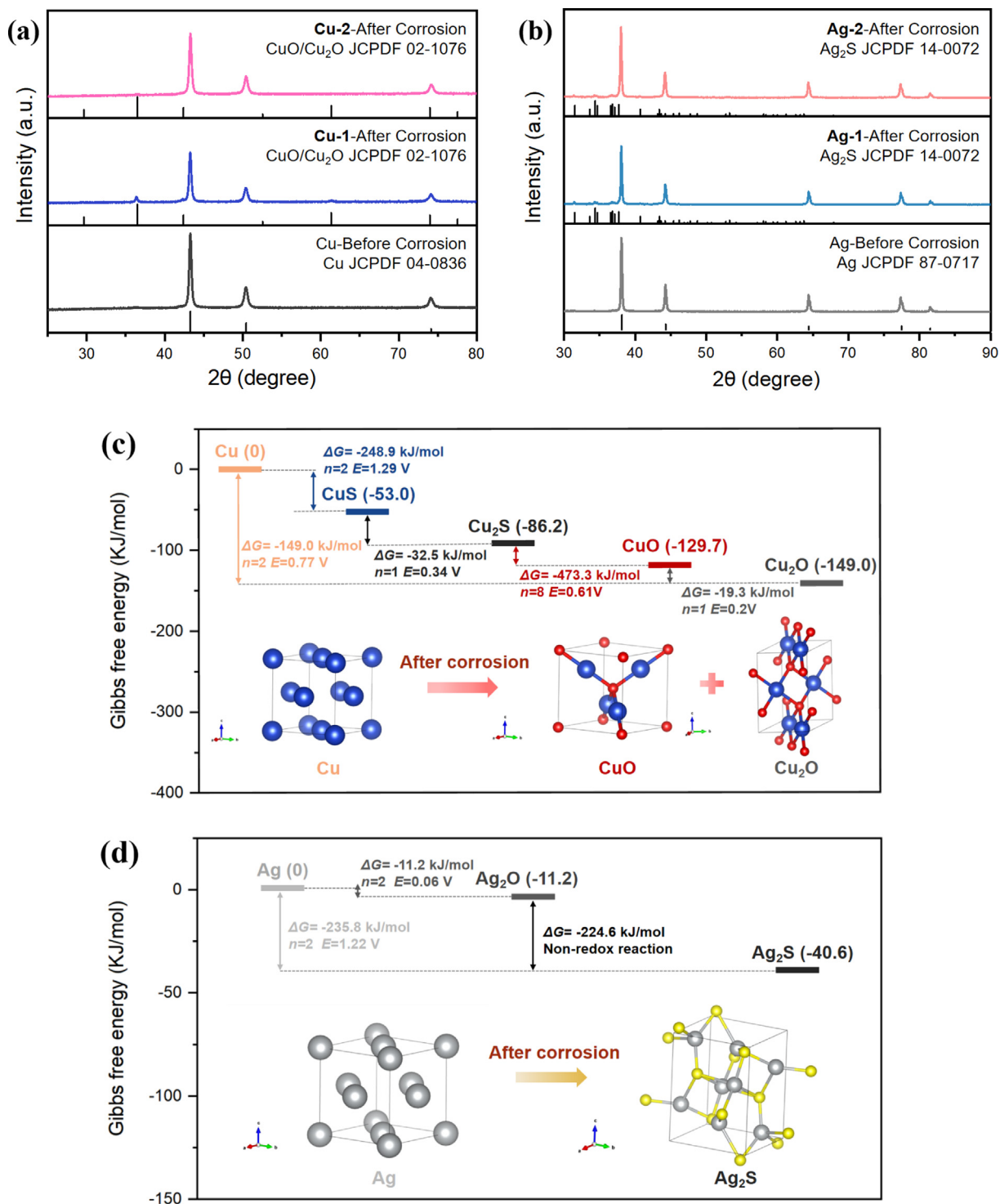

Fig. 12 — XRD test results of the sintered structures before and after corrosion: (a)Cu-1 and Cu-2; (b)Ag-1 and Ag-2. Possible reactions of the sintered (c)copper and (d)silver during corrosion.
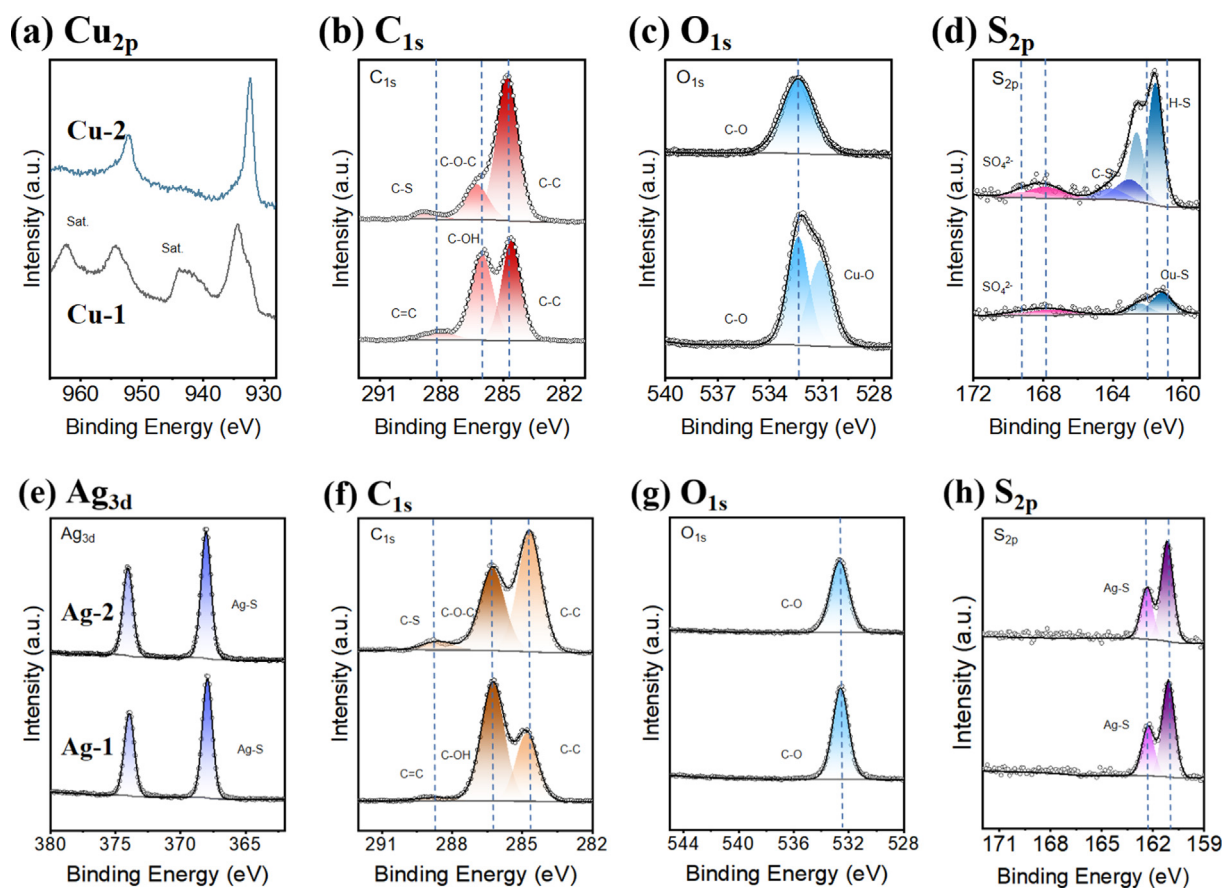
Fig. 13 — (a) Cu 2p, (b) C 1s, (c) O 1s, (d) S 2p XPS spectra of sintered copper after corrosion; (e) Ag 2p, (f) C 1s, (g) O 1s, (h) S 2p XPS spectra of sintered silver after corrosion.

$2p_{1/2}$) in the S 2p spectrum should be assigned to the Cu—S bond of CuS, indicating that a trace amount of CuS also appeared on the reacted surface [35]. Nevertheless, for the corroded Cu-2 sample surface, the XPS results showed that neither copper oxides nor sulfides were formed on the surface.

The peaks at 161.3 eV (S $2p_{3/2}$) and 162.8 eV (S $2p_{1/2}$) in the S 2p XPS spectrum corresponded to the S—H bond [36], and that at 163.0 eV (S $2p_{3/2}$) and 164.3 eV (S $2p_{1/2}$) were assigned to C—S [37], illustrated that epoxy resin in Cu-2 sample may have reacted with H_2S. The peak at 288.9 eV in the C 1s XPS
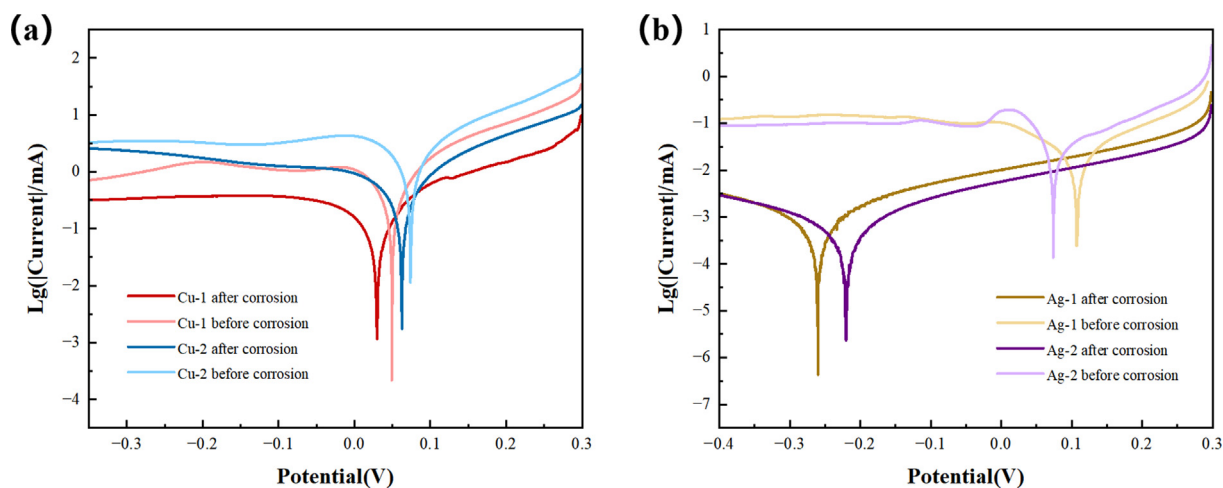

Fig. 14 — The polarization curves of (a) copper-based sintered paste and (b) silver-based sintered paste before and after corrosion.

Table 6 − The characteristic parameters obtained by polarization curves of copper-based sintered paste and silver-based sintered paste before and after corrosion.

Samples	β_a	$I_{corr,a}$ (mA)	β_c	$I_{corr,c}$ (mA)	E_0 (V)	E_c (V)	I_{corrr} (mA)	R_p/Ω
Cu-1-Before corrosion	0.054	0.546	−0.0524	0.507	0.049	0.047	0.526	7.930
Cu-1-After corrosion	0.0493	0.277	−0.1035	0.34	0.029	0.036	0.318	18.547
Cu-2-Before corrosion	0.0784	1.029	−0.0759	0.975	0.074	0.071	1.002	18.563
Cu-2-After corrosion	0.0465	0.443	−0.0606	0.467	0.063	0.064	0.457	46.800
Ag-1-Before corrosion	0.0676	0.137	−0.0777	0.147	0.107	0.109	0.142	4.655
Ag-1-After corrosion	0.0525	0.025	−0.0596	0.025	−0.26	−0.259	0.025	4.159
Ag-2-Before corrosion	0.1264	0.191	−0.0556	0.211	0.074	0.077	0.197	12.567
Ag-2-After corrosion	0.0649	0.024	−0.0652	0.023	−0.22	−0.221	0.024	3.625

spectrum (Fig. 13(b)) also proved the existence of the C−S bond [38]. After corrosion, both samples presented peaks at 167.9 eV (S $2p_{3/2}$) and 169.2 eV (S $2p_{1/2}$) that were attributed to SO_4^{2-}, produced by the oxidation of H_2S [39]. To sum up, the addition of epoxy to the sintered copper paste effectively prevented further oxidation and corrosion of copper, as the

epoxy on the surface reacted with H_2S first in the corrosion environment.

The corroded surfaces of sintered silver samples were also ingested through XPS, as illustrated in Fig. 13(e)−(h). The Ag 3d, O 1s, and S 2p XPS spectra of sintered Ag-1 and Ag-2 samples displayed similar peak shapes. The Ag 3d XPS
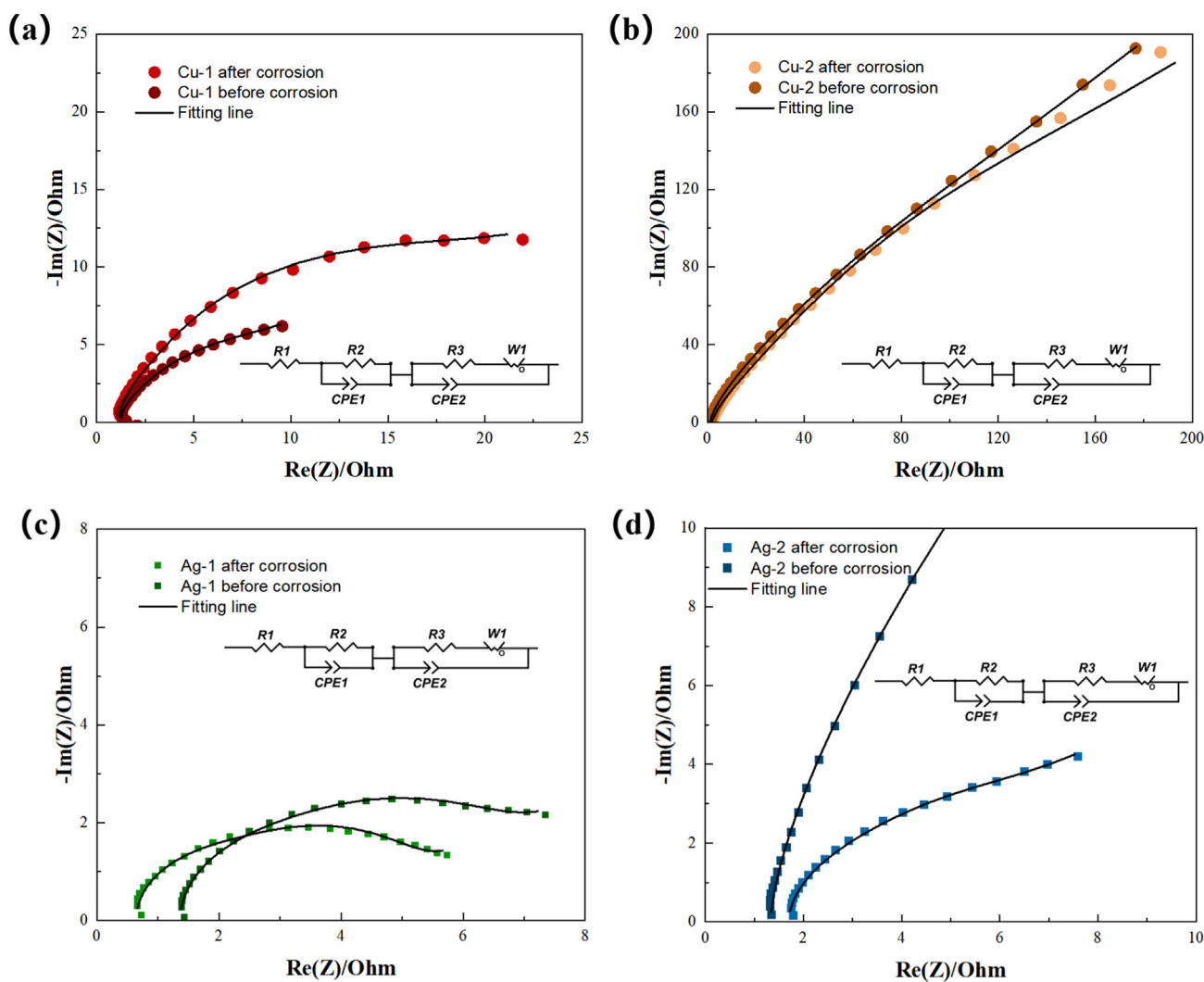
Fig. 15 − Initial EIS spectra of (a) Cu-1, (b) Cu-2, (c) Ag-1, and (d) Ag-2 sintered pastes before and after corrosion. An inset equivalent circuit of $R_1(CPE_1R_2)$ $(CPE_2 (R_3W_1))$ is used to simulate the resistances. Among them, R_1 is the ohmic resistance of the solution, R_2 and R_3 are the charge-transfer resistance of samples, CPE_1 and CPE_2 are the double-layer capacitance, and W_1 is the Warburg impedance.

spectrum (Fig. 13(e)) indicated the presence of two peaks at 368.0 eV (Ag 3d$_{5/2}$) and 373.9 eV (Ag 3d$_{3/2}$), which corresponded to the silver compound [40]. The S 2p XPS spectrum (Fig. 13(h)) exhibited two peaks at 161.1 eV (S 2p3/2) and 162.3 eV (S 2p1/2), which were well-matched to the Ag−S bond of Ag$_2$S [40]. The XRD results confirmed the presence of Ag$_2$S as the primary corrosion product. However, no sulfate traces were detected in the S 2p XPS spectrum. Moreover, the C−S bond was also observed in the C 1s XPS spectrum (Fig. 13(f)). In conclusion, distinct peaks of Ag$_2$S were observed on the surfaces of both sintered Ag-1 and Ag-2 samples, and evidence of the reaction of epoxy resin with H$_2$S was found only in the Ag-2 sample.

3.4.   Electrochemical analysis

To investigate the influence of epoxy resin addition and the appearance of corrosion products on further corrosion, an electrochemical analysis was employed. Fig. 14 illustrates the polarization curves of sintered copper and sintered silver flake samples, both before and after H$_2$S gas corrosion. The corresponding values calculated from the polarization curves, including anodic and cathodic Tafel slopes (β_a and β_c respectively), corrosion potentials (E_{corr}), and corrosion current densities (I_{corr}) are presented in Table 6.

It was observed that the E_{corr} of both sintered copper and sintered silver samples shifts to a negative potential direction after H$_2$S corrosion. This change in thermodynamic corrosion tendency was mainly caused by the destruction of the dense structure on the surface of the samples. Additionally, the I_{corr} of the sintered paste displayed a downward trend after corrosion, mainly due to the formation of porous corrosion products with low electronic conductivity on the surface. These products were not conducive to further electrochemical corrosion reaction, leading to a kinetic decline in reaction rate. It is noteworthy that the change in β_a before and after corrosion was more significant than that of β_c, indicating that the corrosion mainly occurred in the anode (i.e., the sintered paste sample). Interestingly, the change in E_{corr} of sintered copper

before and after corrosion was much smaller than that of sintered silver, suggesting that the former had a significant advantage in corrosion resistance. Furthermore, it showed a higher E_{corr} for Cu-2 and Ag-2 after corrosion, benefiting from the physical anti-corrosion protection provided by the epoxy resin.

To further explore the corrosion resistance (R_p) of sintered copper and sintered silver samples, the electrochemical impedance spectroscopy (EIS) tests were conducted on each sample, both before and after corrosion. The results are shown in Fig. 15. The transfer resistances for sintered copper samples increased after corrosion (Fig. 15(a−b)). This increase suggests that the attachment of corrosion products on the surface may have inhibited further corrosion reactions. Conversely, the sintered silver samples exhibited the opposite trend after corrosion (Fig. 15(c−d)). This phenomenon confirms the excellent corrosion resistance of sintered copper. Additionally, it is noteworthy that both Cu-2 and Ag-2 samples, which have better physical and chemical stability due to the epoxy resin, show better corrosion resistance than Cu-1 and Ag-1 samples. This observation is also consistent with the polarization curve analysis.

3.5.   Molecular dynamics simulations

In order to investigate the interaction between organic residues and sintered copper or silver surfaces, the corrosion behavior of four samples was simulated using molecular dynamics simulation under high-humidity-H$_2$S conditions, as depicted in Fig. 16. The statistical results of corrosion behavior are presented in Fig. 17, wherein (b), (d), (f) and (h) demonstrate the relationship between the diffusion depth of the corrosive elements (S, O) and simulation time. The simulation time was observed to be 200 ps, during which all four systems were found to be fundamentally stable and were thus selected for subsequent simulation analysis. Moreover, the slopes of the Cu models in Fig. 17 (b), (d), (f), and (h) were generally higher than those of the Ag models, indicating a rapid
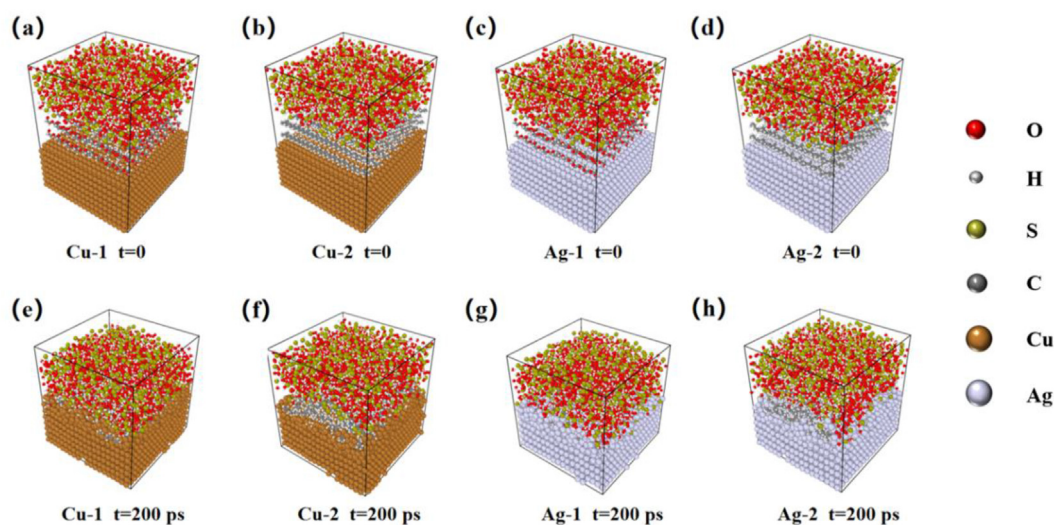

Fig. 16 − (a)−(d) The initial configurations of the simulation model. (e)−(h) Configurations after corrosion simulation (200 ps). (Red is oxygen, white is hydrogen, yellow is sulfur, black is carbon, brown is copper, and gray is silver.).
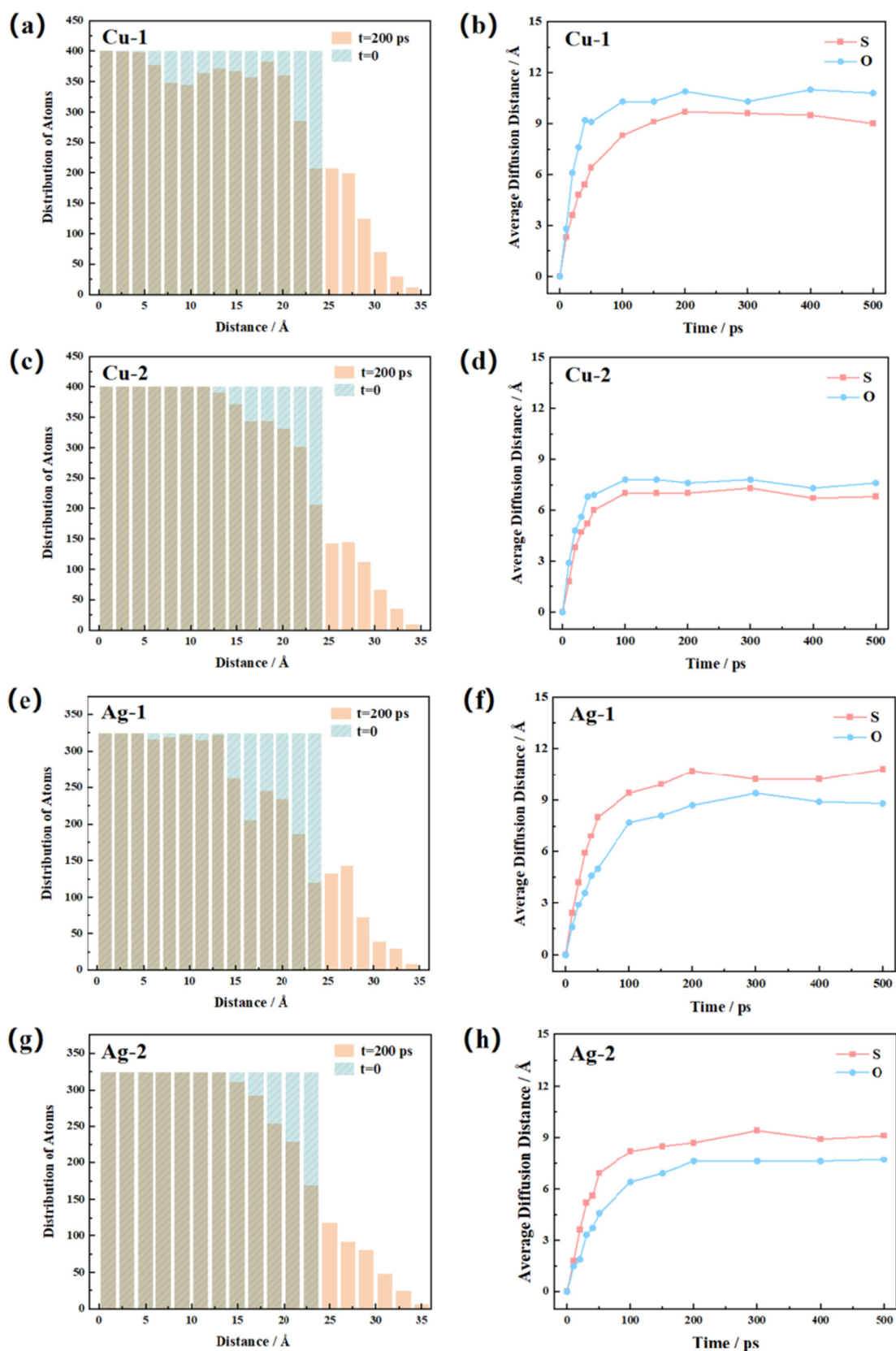
Fig. 17 − Initial and last distribution (t = 200 ps) of Cu in models for (a)Cu-1 and (c)Cu-2. Initial and last distribution (t = 200 ps) of Ag in models for (e)Ag-1 and (g)Ag-2. (b), (d), (f), and (h) Average diffusion distance of elements S and O.
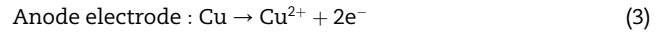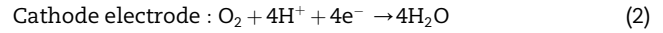
generation of a stable diffusion depth for the reactions between copper and corrosive medium. The conclusion is consistent with the order of metal activity, thereby validating the rationality of the model.

Fig. 17 (a), (c), (e), and (g) depicted the initial and final distributions of copper or silver in each model after 200 ps. It is evident that the samples coated with epoxy resin (Cu-2, Ag-2) retained more metal atoms. Furthermore, the analysis of S and O reaction-diffusion depth indicated the occurrence of both oxidation and vulcanization reactions. In the case of copper, the oxidation trend was more pronounced, while for silver, the vulcanization reaction played a dominant role, which was consistent with the experimental findings of corrosion product characterization. Simultaneously, simulation results revealed that the reaction depths of Cu-1 and Ag-1 without epoxy resin were 10.5 Å, whereas, for Cu-2 and Ag-2 with epoxy resin, they were approximately 8 Å and 9 Å, respectively. The results reaffirmed the protective effect of epoxy resin against corrosion, and the anti-corrosion effect on copper was more significant due to the shallower corrosion depth.

3.6. Corrosion mechanism analysis

Based on previous observations and analyses, this study speculates on the corrosion mechanism of four types of chip connection materials in the high-humidity (85% RH)-H_2S (100 ppb) environment. The speculated schematic diagram of the corrosion process is shown in Fig. 18. When samples were placed in the gas corrosion test chamber, a water film formed on their surfaces due to high humidity, as shown in Fig. 18(a). Trace amounts of oxygen from the air dissolved in the water film, while hydrogen sulfide also dissolved and ionized H^+, HS^-, and S^{2-}. For the surface of sintered copper (Fig. 18(b)), oxygen-absorbing corrosion mainly occurred, as shown in Eqs. (2) and (3).

$$\text{Cathode electrode}: O_2 + 4H^+ + 4e^- \rightarrow 4H_2O \qquad (2)$$

$$\text{Anode electrode}: Cu \rightarrow Cu^{2+} + 2e^- \qquad (3)$$

Cu^{2+} ions and S^{2-} formed insoluble CuS. CuS was then converted into more stable copper oxides (CuO/Cu_2O) due to the presence of oxygen. The electrical conductivity of CuO/Cu_2O is poor, so their production in large quantities significantly reduced the conductivity. The structure of copper oxides is loose, leading to a noticeable decrease in the shear strength. In addition, it is worth mentioning that copper oxide is an excellent catalyst and is sensitive to H_2S [41]. Afterward, H_2S enriched on the surface of the sintered copper was oxidized by oxygen in the air under the catalysis of the generated oxide [42–44]. Thus, the SO_4^{2-} detected in the XPS test was generated. However, with the accumulation of copper oxides, more H_2S reacted with O_2 instead of ionizing in water to produce S^{2-}. Therefore, the process of generating CuS was effectively suppressed, and the corresponding process of copper loss of electrons and the process of generating oxides
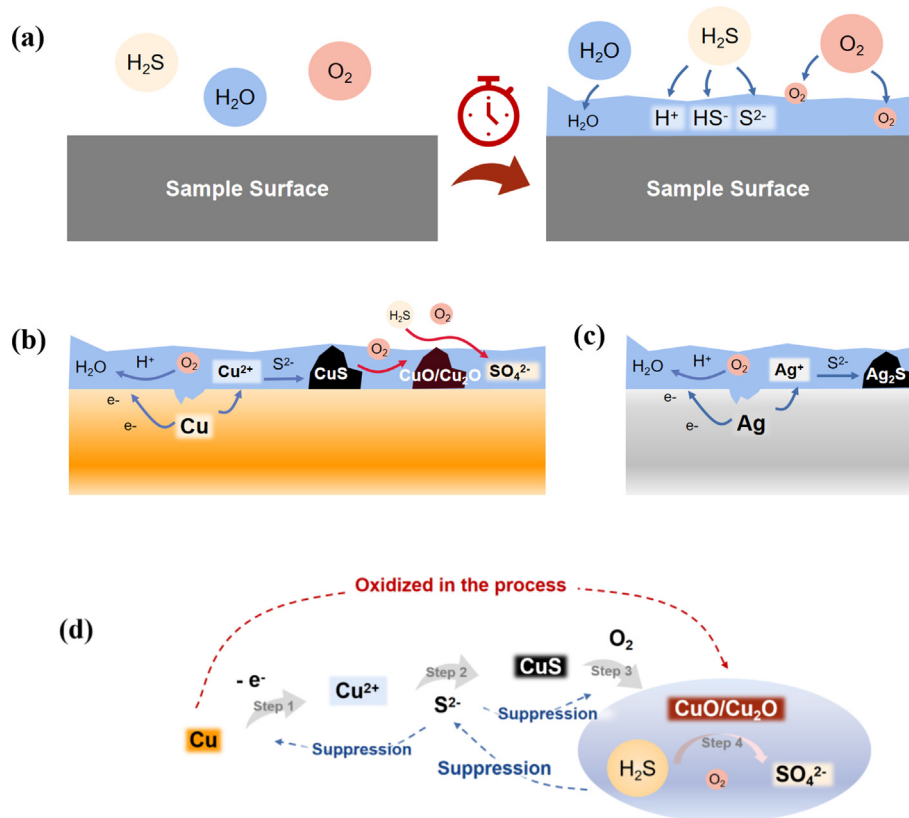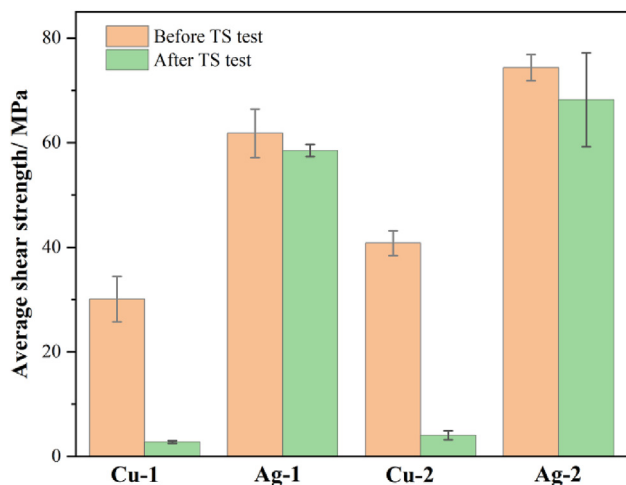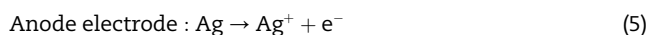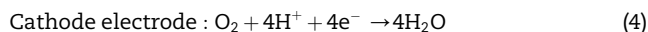

Fig. 18 — Schematic diagram of (a)changes in the surface of the sample after the corrosion; (b)corrosion mechanism of sintered copper surface; (c)corrosion mechanism of sintered silver surface; (d)the mechanism of copper oxide to further suppress copper corrosion.

Fig. 19 — **Average shear strength of the sintered joints before and after temperature shock.**

The generated silver ions reacted with S^{2-} to form Ag_2S solid deposit. However, as shown in Fig. 11(d) for the Gibbs free energy calculation, Ag_2S is highly stable. Therefore, Ag_2S does not react further with oxygen and is easily formed. In addition, Ag_2S formed a dense layer on the surface of the silver. The observed increase in shear strength, despite the occurrence of corrosion, is believed to be a result of the formation of the Ag/Ag_2S interfaces and the porous structure in the sintered silver material. This suggests that the corrosion process does not necessarily lead to a deterioration of the material's mechanical properties. The Ag/Ag_2S interfaces, which formed due to the reaction between the silver and sulfur species in the corrosive environment, may contribute to the enhanced strength by acting as a barrier that impedes the propagation of cracks. Furthermore, the porous structure that arises during the sintering process can act as a stress concentrator, which increases the local strength of the material. Moreover, the corrosion rate of the silver inside with epoxy protection was slowed down. The effect of epoxy resin in sintered silver was commonly reflected in enhancement shear strength and the reduction of electrical conductivity.

3.7. Reliability analysis under thermal shock

For the WBG power modules, the actual operating temperature usually switches from room temperature up to 150 °C Therefore, it is crucial to conduct further research on the corroded joint reliability under thermal shock testing regarding the performance of the four types of joints. In this study, four groups of joints aged by H_2S as mentioned in Section 2.1.3 were further tested based on the JESD22-A104
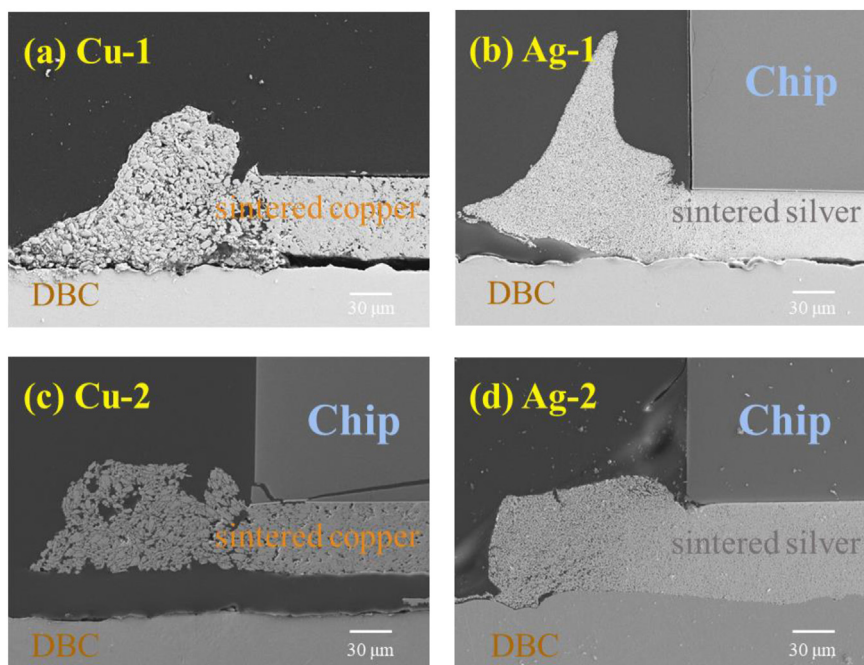
was also inhibited, as shown in Fig. 18(d). Under this assumption, the corrosion process of copper was gradually slowed down. For the Cu-2 sample, the addition of epoxy resin effectively prevented contact between the copper surface and the corrosive medium. The small amount of H_2S reaching the surface first reacted with the surface oxide generated in the process, avoiding the corrosion of the internal copper and achieving an evident anti-corrosion effect. Similarly, Fig. 18(c) illustrated the corrosion mechanism of the sintered silver surface. Like sintered copper, oxygen-absorbing corrosion also dominated, as shown in Eqs. (4) and (5).
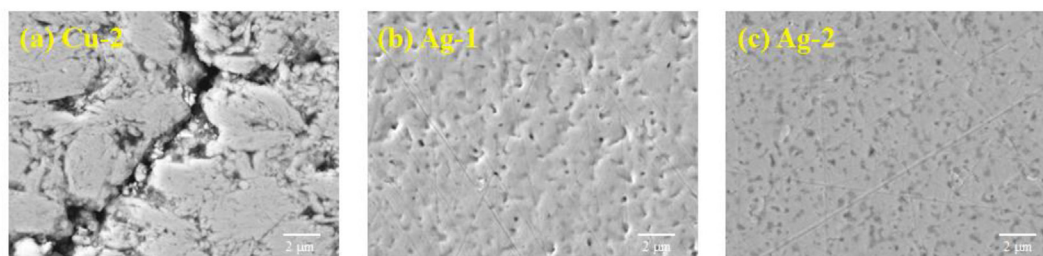
$$\text{Cathode electrode}: O_2 + 4H^+ + 4e^- \rightarrow 4H_2O \qquad (4)$$

$$\text{Anode electrode}: Ag \rightarrow Ag^+ + e^- \qquad (5)$$

Fig. 20 — **SEM photos of the joints after thermal shock (a)Cu-1; (b)Ag-1; (c)Cu-2; (d)Ag-2.**

Fig. 21 — SEM photos of the sintered layer in the joints after thermal shock (a)Cu-2; (b)Ag-1; (c)Ag-2.

standard, with a total of 500 temperature cycles within a range of −50 to 150 °C, with a cycling rate of 2 cycles per hour.

The reliability evaluation of such sintered joints was primarily based on the shear strength indicator. Fig. 19 compared the average shear strength of the sintered joints before and after the thermal shock tests. The shear strength of Cu-1 and Cu-2 samples exhibited a significant decrease, dropping from 30.10 MPa to 40.81 MPa—2.75 MPa and 4.06 MPa, respectively. This corresponds to a change range of 90.86% and 90.06%. In contrast, the decrease in the shear strength of the Ag-1 and Ag-2 samples was only 5.32% and 8.28%, respectively. Therefore, it is concluded that silver sintered joints demonstrated excellent thermal shock resistance based on the changes in shear strength.

Furthermore, the morphology changes of the joint samples after thermal shock were analyzed using SEM, as depicted in Figs. 20 and 21. After thermal shocks, significant cracks were observed at the interface between the sintered layer and the DBC substrate in the copper-sintered joints as shown in Fig. 20 (a) and (c). Moreover, the chip of the Cu-1 sample even detached (Fig. 20 (a)), and cracks appeared in the sintered layer of the Cu-2 sample (Fig. 21(a)). Such failure is speculated to the extensive copper oxidation during the H_2S corrosion, which leads to a high coefficient of thermal expansion (CTE) mismatch with copper and copper-related corrosion products during thermal cycling tests. In contrast, Ag_2S was reported to share a similar CTE with Ag. Therefore, Ag-1 and Ag-2 showed better thermal shock resistance. Moreover, the cross section morphology changes in silver joints were much less pronounced (Fig. 20 (b) and (d), Fig. 21 (b) and (c)). It is worth mentioning that the shear strength decrease of the Ag-2 sample was slightly higher than that of the Ag-1 sample. It is hypothesized that this strength decrease is due to the thermal mismatch caused by the epoxy filling. These findings provided an evaluation of the rusted sintered joints' reliability regarding thermal shock tests, that silver joints exhibited less shear strength decrease compared to copper joints.

4. Conclusions

In this work, a comparison was made between epoxy-free solvent systems and epoxy-added solvents for sintered copper and sintered silver, respectively, to investigate their aging behavior under high-humidity (85% RH)-H_2S (100 ppb)

corrosion conditions. The mechanisms of the corrosion were analyzed using XRD, XPS, SEM, electrochemical measurements, and ReaxFF-MD simulation. The main conclusions are summarized as follows.

(1) The addition of epoxy resin to sintered copper joints evidently prevented the corrosion of both the surface and interior, resulting in an improvement in the electrical conductivity to 7.99×10^4 S/cm after the reaction. The shear strength of Cu-2 with epoxy resin increased after corrosion, while decreased for Cu-1 without epoxy. However, the connection strength and mechanical reliability of corroded sintered copper joints under thermal shock need to be further enhanced. For sintered silver samples, the anti-corrosion effect of the epoxy resin on the joints was not obvious, while the enhancement of the epoxy on the shear strength was significant. Moreover, corroded silver sintered joints exhibited excellent thermal shock resistance, which indicates additives through solvent adjustment could be prosperous for future work to enhance its corrosion resistance.

(2) Oxygen-absorbing corrosion was dominated in both sintered copper and silver. The results of EDS, XRD, XPS spectra, and the calculation on Gibbs free energy of reactions indicated that the reaction product of the sintered copper was mainly the mixture of CuO and Cu_2O converted by CuS, while the reaction product of the sintered silver was predominantly Ag_2S.

(3) The results of electrochemical testing and ReaxFF-MD simulation demonstrated that the presence of epoxy resin effectively reduced the occurrence of corrosion. In addition, for copper, the transfer resistances after corrosion suggested that the attachment of corrosion products on the surface could inhibit further corrosion reactions.

This study focused on the optimization of the anti-corrosion behavior of sintered die-attach materials, particularly in the comparison of sintering copper and silver, with the addition of epoxy resin. This research is highly relevant to practical off-shore applications, especially for accelerating the adoption of sintering materials in power modules. Further investigations could be conducted to explore the influence of varying amounts and types of epoxy resin on the corrosion protection of the joints, and the improvement of the reliability performance for corroded sintered joints.

Credit authorship contribution statement

Xinyue Wang: Methodology, Experiments, Data collection and analysis, Writing - original draft. **Zhoudong Yang:** Technical support on characterization experiments, Data analysis. **Boya Wang:** Technical support on characterization experiments, Data analysis. **Wei Chen:** Aging experiments. **Guoqi Zhang:** Supervision. **Jing Zhang:** Supervision, Writing - review & editing. **Jiajie Fan:** Supervision, Writing - review & editing. **Pan Liu:** Conceptualization, Methodology, Writing - review & editing, Project administration, Funding acquisition, Supervision.

Declaration of competing interest

The authors declare that they have no known competing financial interests or personal relationships that could have appeared to influence the work reported in this paper.

Acknowledgments

REFERENCES

[1] Hou F, Wang W, Cao L, Li J, Su M, Lin T, Zhang G, Ferreira B. Review of packaging schemes for power module. IEEE Journal of Emerging and Selected Topics in Power Electronics 2020;8:223–38. https://doi.org/10.1109/jestpe.2019.2947645.

[2] Lee H, Smet V, Tummala R. A review of SiC power module packaging technologies: challenges, advances, and emerging issues. IEEE Journal of Emerging and Selected Topics in Power Electronics 2020;8:239–55. https://doi.org/10.1109/jestpe.2019.2951801.

[3] Yadlapalli RT, Kotapati A, Kandipati R, Balusu SR, Koritala CS. Advancements in energy-efficient GaN power devices and power modules for electric vehicle applications: a review. Int J Energy Res 2021;45:12638–64. https://doi.org/10.1002/er.6683.

[4] Seal S, Mantooth H. High performance silicon carbide power packaging—past trends, present practices, and future directions. Energies 2017;10. https://doi.org/10.3390/en10030341.

[5] Mantooth HA, Ahmed S, Ang SS. Power semiconductor device modeling and simulation. ECS Trans 2013;58:391–8. https://doi.org/10.1149/05804.0391ecst.

[6] Wang X, Zeng Z, Zhang G, Zhang J, Liu P. Joint analysis and reliability test of epoxy-based nano silver paste under different pressure-less sintering processes. J Electron Packag 2021;144. https://doi.org/10.1115/1.4053432.

[7] Manikam VR, Razak KA, Cheong KY. A novel silver–aluminium high-temperature die attach nanopaste system: the effects of organic additives content on post-sintered attributes. J Mater Sci Mater Electron 2013;24:2678–88. https://doi.org/10.1007/s10854-013-1155-9.

[8] Kim D, Nagao S, Chen C, Wakasugi N, Yamamoto Y, Suetake A, Takemasa T, Sugahara T, Suganuma K. Online thermal resistance and reliability characteristic monitoring of power modules with Ag sinter joining and Pb, Pb-free solders during power cycling test by SiC TEG chip. IEEE Trans Power Electron 2021;36:4977–90. https://doi.org/10.1109/tpel.2020.3031670.

[9] Guo W, Zeng Z, Zhang X, Peng P, Tang S. Low-temperature sintering bonding using silver nanoparticle paste for electronics packaging. J Nanomater 2015:1–7. https://doi.org/10.1155/2015/897142. 2015.

[10] Szałapak J, Kiełbasiński K, Dybowska-Sarapuk Ł, Krzeminski J, Teodorczyk M, Kowaluk T, Jakubowska M. Influence of carbon nanoparticles additives on nanosilver joints in LTJT Technology. J Electron Packag 2021;143. https://doi.org/10.1115/1.4049240.

[11] Kiełbasiński K, Szałapak J, Jakubowska M, Młożniak A, Zwierkowska E, Krzemiński J, Teodorczyk M. Influence of nanoparticles content in silver paste on mechanical and electrical properties of LTJT joints. Adv Powder Technol 2015;26:907–13. https://doi.org/10.1016/j.apt.2015.03.007.

[12] Kos JF. Anomalies in the low-temperature thermal and electrical resistivities of silver. J Phys Condens Matter 1990;2:4859–68. https://doi.org/10.1088/0953-8984/2/22/007.

[13] Li B, Zhao Z, Li M, Wang T, Li H. Reliability evaluation of sintered silver and Sn-3Ag-0.5Cu solder joints using a thermal cycling test. In: 2017 18th international conference on electronic packaging Technology. ICEPT); 2017. https://doi.org/10.1109/icept.2017.8046518. IEEE.

[14] Moore JP, McElroy DL, Graves RS. Thermal conductivity and electrical resistivity of high-purity copper from 78 to 400 K. Can J Phys 1967;45:3849–65. https://doi.org/10.1139/p67-323.

[15] Ishikawa D, An BN, Mail M, Wurst H, Leyrer B, Blank T, Weber M, Nakako H. Die-attach properties of pressure-sintered copper joints on adhesive metallization surfaces in N2 atmosphere. In: 2021 international conference on electronics packaging. ICEP); 2021. https://doi.org/10.23919/icep51988.2021.9451911. IEEE.

[16] Suzuki T, Yasuda Y, Terasaki T, Morita T, Kawana Y, Ishikawa D, Nishimura M, Nakako H, Kurafuchi K. Macro- and micro-deformation behavior of sintered-copper die-attach material. IEEE Trans Device Mater Reliab 2018;18:54–63. https://doi.org/10.1109/tdmr.2017.2787756.

[17] Chijioke JN, Kiray V. A review of power electronics applications for wind energy systems in microgrids. Journal of Scientific Research and Reports 2020:139–48. https://doi.org/10.9734/jsrr/2020/v26i430254.

[18] Trapani K, Millar DL, Smith HCM. Novel offshore application of photovoltaics in comparison to conventional marine renewable energy technologies. Renew Energy 2013;50:879–88. https://doi.org/10.1016/j.renene.2012.08.043.

[19] Kolbinger E, Wagner S, Gollhardt A, Rämer O, Lang KD. Corrosion behaviour of sintered silver under maritime environmental conditions. Microelectron Reliab 2018;88–90:715–20. https://doi.org/10.1016/j.microrel.2018.07.123.

[20] Ek A, Sk A, Sw A, Sr By. Investigation of the mechanical properties of corroded sintered silver layers by using Nanoindentation. Microelectronics Reliability; 2020. https://doi.org/10.1016/j.microrel.2020.113889.

[21] Hussien BM, Rabeea MA, Farhan MM. Characterization and behavior of Hydrogen Sulfide plumes released from active sulfide-tar springs, Hit-Iraq. Atmos Pollut Res 2020;11:894–902. https://doi.org/10.1016/j.apr.2020.02.001.

[22] Zhang W, Zhao Y, Zhang P, Hao Y, Yu S, Min L, Li L, Ma D, Chen L, Yi B, Tang X, Meng Q, Liu L, Wang S, Shen W,

Zhang H. Decrease in male mouse fertility by hydrogen sulfide and/or ammonia can Be inheritable. Chemosphere 2018;194:147—57. https://doi.org/10.1016/j.chemosphere.2017.11.164.

[23] Cichowicz R, Dobrzański M. Spatial analysis (measurements at heights of 10 m and 20 m above ground level) of the concentrations of particulate matter (PM10, PM2.5, and PM1.0) and gaseous pollutants (H2S) on the university campus: a case study. Atmosphere 2021;12:62. https://doi.org/10.3390/atmos12010062.

[24] Lin SH, Chuang TS. Corrosion of PC boards in contaminated industrial environment. Appl Surf Sci 1994;74:323—30. https://doi.org/10.1016/0169-4332(94)90114-7.

[25] Hu D, Gu T, Cui Z, Vollebregt S, Fan X, Zhang G, Fan J. Insights into the high-sulphur aging of sintered silver nanoparticles: an experimental and ReaxFF study. Corrosion Sci 2021;192. https://doi.org/10.1016/j.corsci.2021.109846.

[26] Medgyes B, Illés B, Harsányi G. Electrochemical migration behaviour of Cu, Sn, Ag and Sn63/Pb37. J Mater Sci Mater Electron 2011;23:551—6. https://doi.org/10.1007/s10854-011-0435-5.

[27] Xiangquan F, Wang T, Yuqi C, Binhai Z, Jiaji W. Oxidation study of copper wire bonding. In: 2010 11TH international conference on electronic packaging technology & high density packaging. ICEPT-HDP); 2010. https://doi.org/10.1109/icept.2010.5582431. IEEE.

[28] Jeong H, Myung WR, Sung YG, Kim KY, Jung SB. Effect of epoxy on mechanical property of SAC305 solder joint with various surface finishes under 3-point bend test. J Nanosci Nanotechnol 2018;18:6316—20. https://doi.org/10.1166/jnn.2018.15624.

[29] Jung K-H, Min KD, Lee C-J, Park B-G, Jeong H, Koo J-M, Lee B, Jung S-B. Effect of epoxy content in Ag nanoparticle paste on the bonding strength of MLCC packages. Appl Surf Sci 2019;495. https://doi.org/10.1016/j.apsusc.2019.07.229.

[30] Hwang B-U, Jung K-H, Min KD, Lee C-J, Jung S-B. Pressureless Cu—Cu bonding using hybrid Cu—epoxy paste and its reliability. J Mater Sci Mater Electron 2021;32:3054—65. https://doi.org/10.1007/s10854-020-05055-2.

[31] Duin A, Dasgupta S, F.J.T.j.o.p.c. Lorant, A.. Molecules, spectroscopy, kinetics, environment, g. theory. ReaxFF: A Reactive Force Field for Hydrocarbons; 2001. p. 105. https://doi.org/10.1021/jp004368u.

[32] Dean JA. Lange's Handbook of Chemistry. fifteenth ed. New York, USA: McGraw-Hill; 1999. http://refhub.elsevier.com/S0010-938X(21)00612-0/sbref31.

[33] Okada K, Kotani A. Intersite coulomb interactions in quasi-one-dimensional copper oxides. J Phys Soc Jpn 1997;66:341—4. https://doi.org/10.1143/jpsj.66.341.

[34] Sivkov DV, Petrova OV, Nekipelov SV, Vinogradov AS, Skandakov RN, Isaenko SI, Ob'Edkov AM, Kaverin BS, Vilkov IV, Korolev RI, Sivkov VN. The identification of Cu—O—C bond in Cu/MWCNTs hybrid nanocomposite by XPS and NEXAFS spectroscopy. Nanomaterials 2021;11:2993. https://doi.org/10.3390/nano11112993.

[35] Kutty TRN. A controlled copper-coating method for the preparation of ZnS-MN DC electroluminescent PowderPhosphors mater. Res Bull 1991;26:399—406. https://doi.org/10.1016/0025-5408(91)90054-.

[36] Wu QF, Yakshinskiy BV, Madey TE. Adsorption and decomposition of H2S on UO2(001). Surf Sci 2003;523:1—11. https://doi.org/10.1016/s0039-6028(02)02401-9.

[37] Lindberg lKHB J, Johansson G, Gelius U, Fahlman A, Nordling C, Siegbahn K. Molecular Spectroscopy by Means of ESCA II. Sulfur compounds. Correlation of electron binding energy with structure. Phys Scripta 1970;1:286—98. https://doi.org/10.1088/0031-8949/1/5-6/020.

[38] Peeling J, Hruska FE, McKinnon DM, Chauhan MS, McIntyre NS. ESCA studies of the uracil base. The effect of methylation, thionation, and ionization on charge distribution. Can. J. Chem.-Rev. Can. Chim. 1978;56:2405—11. https://doi.org/10.1139/v78-393.

[39] Kurmaev EZ, Fedorenko VV, Galakhov VR, Bartkowski S, Uhlenbrock S, Neumann M, Slater PR, Greaves C, Miyazaki Y. Analysis of oxyanion (BO 3 3- , CO 3 2- , SO 4 2- , PO 4 3-, SeO 4 4-) substitution in Y123 compounds studied by X-ray photoelectron spectroscopy. J Supercond 1996;9:97—100. https://doi.org/10.1007/bf00728433.

[40] Krylova V, Dukstiene N. Synthesis and characterization of Ag2S layers formed on polypropylene. J Chem 2013;2013:11. https://doi.org/10.1155/2013/987879.

[41] Ramgir NS, Ganapathi SK, Kaur M, Datta N, Muthe KP, Aswal DK, Gupta SK, Yakhmi JV. Sub-ppm H2S sensing at room temperature using CuO thin films. Sensor Actuator B Chem 2010;151:90—6. https://doi.org/10.1016/j.snb.2010.09.043.

[42] Canning GA, Azzam SA, Hoffman AS, Boubnov A, Alshafei FH, Ghosh R, Ko B, Datye A, Bare SR, Simonetti DA. Lanthanum induced lattice strain improves hydrogen sulfide capacities of copper oxide adsorbents. AIChE J 2021;67. https://doi.org/10.1002/aic.17484.

[43] Zheng X, Li Y, Liang S, Yao Z, Zheng Y, Shen L, Xiao Y, Zhang Y, Au C, Jiang L. Promoting effect of Cu-doping on catalytic activity and SO2 resistance of porous CeO2 nanorods for H2S selective oxidation. J Catal 2020;389:382—99. https://doi.org/10.1016/j.jcat.2020.06.010.

[44] Yasyerli S, Dogu G, Ar I, Dogu T. Activities of copper oxide and Cu—V and Cu—Mo mixed oxides for H2S removal in the presence and absence of hydrogen and predictions of a deactivation model. Ind Eng Chem Res 2001;40:5206—14. https://doi.org/10.1021/ie0010621.